Studying Micro to Millisecond Protein Dynamics Using Simple Amide ^{15}N CEST Experiments Supplemented with Major-State R_2 and Visible Peak-position Constraints

Nihar Pradeep Khandave[1], **Ashok Sekhar**[2], **Pramodh Vallurupalli**[1,*]

[1]Tata Institute of Fundamental Research Hyderabad, 36/P, Gopanpally Village, Serilingampally Mandal, Ranga Reddy District, Hyderabad 500046

[2]Molecular Biophysics Unit, Indian Institute of Science, Bengaluru - 560012, Karnataka, India

Abstract

Over the last decade amide ^{15}N CEST experiments have emerged as a popular tool to study protein dynamics that involves exchange between a 'visible' major state and sparsely populated 'invisible' minor states. Although initially introduced to study exchange between states that are in slow exchange with each other (typical exchange rates of, ~10 to ~400 s^{-1}), they are now used to study interconversion between states on the intermediate to fast exchange timescale while still using low to moderate (~5 to ~300 Hz) 'saturating' B_1 fields. The ^{15}N CEST experiment is very sensitive to exchange as the exchange delay T_{EX} can be quite long (~0.5 s) allowing for a large number of exchange events to occur making it a very powerful tool to detect minor sates populated (p_{minor}) to as low as 1%. When systems are in fast exchange and the ^{15}N CEST experiments readily detect the minor states, the exchange parameters are often still poorly defined because the χ^2_{red} versus p_{minor} and χ^2_{red} versus exchange rate (k_{ex}) plots can be quite flat with shallow or no minima and the analysis of such ^{15}N CEST data can lead to wrong estimates of the exchange parameters due to the presence of 'spurious' minima. Here we show that the inclusion of experimentally derived constraints on the intrinsic transverse relaxation rates and the inclusion of visible state peak-positions during the analysis of amide ^{15}N CEST data acquired with moderate B_1 values (~50 to ~300 Hz) results in a convincing minimum in the χ^2_{red} versus p_{minor} and the χ^2_{red} versus k_{ex} plots even when exchange occurs on the ~100 μs timescale. The utility of this strategy is demonstrated on the fast-folding *Bacillus stearothermophilus* peripheral subunit binding domain that folds with a rate constant ~10,000 s^{-1}. Here the analysis of ^{15}N CEST data alone results in χ^2_{red} versus p_{minor} and χ^2_{red} versus k_{ex} plots that contain shallow minima, but the inclusion of visible-state peak positions and restraints on the intrinsic transverse relaxation rates of both states during the analysis of the ^{15}N CEST data results in pronounced minima in the χ^2_{red} versus p_{minor} and χ^2_{red} versus k_{ex} plots and precise exchange parameters even in the fast exchange regime $k_{ex}/|\Delta\omega| \sim 5$). Using this strategy we find that the folding rate constant of PSBD is invariant (~10,500 s^{-1}) from 33.2 to 42.9 °C while the unfolding rate (~70 to ~500 s^{-1}) and unfolded state population (~0.7 to ~4.3%) increase with temperature. The results presented here show that protein dynamics occurring on the ~10 to ~10,000 s^{-1} timescale can be studied using amide ^{15}N CEST experiments.

*Corresponding author: Pramodh Vallurupalli: pramodh@tifrh.res.in.

Keywords

Chemical Exchange; Conformational Exchange; Chemical Exchange Saturation Transfer; CEST;
Protein dynamics; Fast-folding; PSBD

Introduction

Protein molecules interconvert among a wide array of conformational states over a broad
range of timescales varying from picoseconds to seconds (Bahar, Jernigan, and Dill, 2017;
Karplus, 2000). Conformational dynamics occurring over the μs to second time-scale
often involves a dominant major conformational state that exchanges with various sparsely
populated states. Owing to their low populations and short lifetimes these sparsely populated
minor states are not visible in standard NMR spectra that contain signals only from the
dominant major state (Cavanagh et al., 2006). Hence the sparsely populated states are
referred to as 'invisible' states while the major state is termed the 'visible' state. As these
sparsely populated invisible states play crucial roles in protein function, folding, misfolding
and aggregation (Bahar, Jernigan, and Dill, 2017; Milojevic et al., 2007; Sekhar and Kay,
2019), various NMR experiments that manipulate the visible state magnetisation to detect
these 'invisible' states have been developed over the past three decades (Anthis and Clore,
2015; Palmer and Koss, 2019; Rangadurai et al., 2019; Sekhar and Kay, 2019; Torchia,
2011; Tugarinov and Clore, 2019; Vallurupalli et al., 2017; Zhuravleva and Korzhnev, 2017).
These include the $R_{1\rho}$ (Palmer and Massi, 2006; Rangadurai et al., 2019), CPMG (Carr-
Purcell-Meiboom-Gill) (Hansen, Vallurupalli, and Kay, 2008; Loria, Rance, and Palmer,
1999a; Palmer, Kroenke, and Loria, 2001), DEST (Dark-state Exchange Saturation Transfer)
(Fawzi et al., 2011; Tugarinov and Clore, 2019) and CEST (Chemical Exchange Saturation
Transfer) (Forsen and Hoffman, 1963; Vallurupalli, Bouvignies, and Kay, 2012; Ward,
Aletras, and Balaban, 2000) classes of experiments. The $R_{1\rho}$, CPMG and CEST class
experiments detect 'invisible' states based on differences in the chemical shifts (Allerhand
and Thiele, 1966) between the major and minor states, while the DEST methodology
exploits differences in the transverse relaxation of rates (Allerhand and Thiele, 1966) using
the visible major state peak to detect 'dark' states that have very large transverse relaxation
rates (Fawzi et al., 2011; Tugarinov and Clore, 2019).

The CEST class of experiments that were first described by Forsen and Hoffman sixty years
ago to study chemical exchange between visible states (Forsen and Hoffman, 1963) have
subsequently been used in imaging (van Zijl and Yadav, 2011; Ward, Aletras, and Balaban,
2000) and to study exchange between a visible major state and sparsely populated minor
state(s) (Vallurupalli, Bouvignies, and Kay, 2012; Vallurupalli et al., 2017; Zhao, Baisden,
and Zhang, 2020). In a typical CEST experiment used to study exchange between a visible
major state (A) and an invisible minor state (B) that are in slow exchange ($A \underset{k_{AB}}{\overset{k_{BA}}{\rightleftharpoons}} B$) with
each other, longitudinal magnetisation is subjected to a weak B_1 field (~5 to ~50 Hz) for
a time exchange time T_{EX} (~300 to 600 ms) and the intensity (I) of the visible peak is
quantified as a function of the offset at which the B_1 field is applied (Palmer and Koss,
2019; Sekhar and Kay, 2019; Vallurupalli et al., 2017). A plot of the normalised intensity

(I/I_0) of the visible state versus the offset (ϖ_{RF}) at which the B_1 field is applied is called the CEST intensity profile and will contain dips at the chemical shifts of both the major state A (ϖ_A) and the minor state (ϖ_B). Here I_0 is the intensity of the visible state in the absence of the T_{EX} delay. The exchange rate ($k_{ex,AB} = k_{AB} + k_{BA}$), the fractional population of the minor state ($p_B = k_{AB}/k_{ex,AB}$), the chemical shift (ϖ_B) and in favourable cases the transverse relaxation rate ($R_{2,B}$) of the minor state can all be obtained by analysing the CEST intensity profiles recorded at two B_1 fields leading to a complete description of the exchange processes and allowing one to reconstruct the spectrum of the 'invisible' state. [15]N and ^{13}C CEST experiments were initially used to detect minor states (Bouvignies and Kay, 2012; Bouvignies, Vallurupalli, and Kay, 2014; Vallurupalli, Bouvignies, and Kay, 2012) that are in slow exchange ($k_{ex,AB}/|\ \omega_{AB}| < \sim0.5$) with the major state, so that separate dips corresponding to major and minor states could be observed in the intensity profiles of at least a few residues. Here, ω_A and ω_B are the resonance frequencies (rad/s) of the spin of interest in states A and B respectively and $\Delta\omega_{AB} = \omega_B - \omega_A$. Similarly (in ppm) we have $\Delta\varpi_{AB} = \varpi_B - \varpi_A$. Due to the limited range of $|\ \omega_{AB}|$ values in protein samples, this requirement for separate major and minor state dips in the CEST intensity profiles limited the applicability of the CEST experiments to protein exchange processes with exchange rates less than ~400 s^{-1}, while CPMG and $R_{1\rho}$ experiments were used to study exchange occurring on the micro to millisecond timescale (Massi et al., 2004; Palmer, Kroenke, and Loria, 2001; Sekhar and Kay, 2013; Zhuravleva and Korzhnev, 2017). When exchange between states A and B lies in the intermediate to fast exchange limit ($\sim0.7 < k_{ex,AB}/|\ \omega_{AB}| < \sim5$) the CEST intensity profile will not contain two distinct dips arising from states A and B, but will contain a single asymmetric dip (Rangadurai, Shi, and Al-Hashimi, 2020). Just as off-resonance $R_{1\rho}$ data (Palmer and Massi, 2006; Rangadurai et al., 2019) has been analysed to study exchange occurring on the intermediate to fast exchange timescale, these asymmetric CEST intensity profiles obtained with larger B_1 values (~100 to ~300 Hz) that lack distinct dips can also be analysed to obtain the exchange parameters ($k_{ex,AB}$ and p_B), minor state chemical shifts etc (Avram et al., 2017; Ramanujam, Charlier, and Bax, 2019; Rangadurai, Shi, and Al-Hashimi, 2020; Tiwari et al., 2021). A particularly pleasing aspect of these CEST experiments is the use of very modest B_1 fields ($< \sim300$ Hz) that are not taxing on the probe to characterise exchange processes occurring at rates on the order of 10,000 s^{-1}. In contrast to $R_{1\rho}$ experiments (Korzhnev, Orekhov, and Kay, 2005; Massi et al., 2004), in the case of CEST experiments there is no need to use intricate schemes to align the magnetisation along the applied B_1 field allowing one to easily use small to moderate B_1 fields at any desired offset and easily collect intensity profiles over a wide chemical shift range. As the T_{EX} delay in a CEST experiment is usually quite long (~0.5 s), several exchange events occur during T_{EX} making them very sensitive to exchange and because the CEST experiments often do not need specially labelled samples, they have been used to study several processes including protein folding, misfolding & aggregation (Goerke et al., 2017; Lim et al., 2014; Sekhar et al., 2015; Tiwari et al., 2021), protein/nucleic acid conformational exchange (Deshmukh et al., 2016; Gladkova et al., 2017; Rangadurai, Shi, and Al-Hashimi, 2020; Zhao et al., 2017), reaction mechanisms (Ramanujam, Charlier, and Bax, 2019; Sekhar et al., 2018) etc to name a few. Consequently new CEST experiments and strategies are continuously being developed, including ones that extend the applicability of CEST experiments to study exchange between multiple states (Tiwari et al., 2021;

Vallurupalli, Tiwari, and Ghosh, 2019), to probe new sites in molecules (Karunanithy, Reinstein, and Hansen, 2020; Pritchard and Hansen, 2019; Tiwari and Vallurupalli, 2020; Yuwen and Kay, 2018; Yuwen, Sekhar, and Kay, 2017), to expedite data analysis (Chao, Zhang, and Byrd, 2021; Karunanithy et al., 2022), to expedite acquisition (Bolik-Coulon, Hansen, and Kay, 2022; Jameson et al., 2019; Leninger et al., 2018; Toyama and Shimada, 2019; Yuwen, Bouvignies, and Kay, 2018; Yuwen, Kay, and Bouvignies, 2018), to deal with artefacts (Tiwari, Pandit, and Vallurupalli, 2019; Xia et al., 2021) etc.

Here we have used ^{15}N CEST experiments with B_1 values ranging from ~50 to ~300 Hz to study the folding of the ~4.7 kDa peripheral subunit binding domain (PSBD) from the pyruvate dehydrogenase multienzyme complex of *Bacillus stearothermophilus* that folds on the ~100 μs timescale (Vugmeyster et al., 2000). Under conditions used here, at 42.9 °C the unfolded (U) state has a population (p_U) of ~4.3% and the exchange rate ($k_{ex,FU}$) between the folded (F) and unfolded (U) state is ~11,739 s^{-1}. The ^{15}N CEST intensity profiles were asymmetric and incompatible with a one-state system but are compatible with a two-state (F$\rightleftharpoons$U) exchange model in which the protein exchanges between the native folded state (F) and the unfolded state (U). Although some ^{15}N | ϖ_{FU}| values were as large as ~8 ppm (~3566 rad/s at 700 MHz), the two-state χ^2_{red} versus p_U and χ^2_{red} versus $k_{ex,FU}$ plots are quite flat and when ^{15}N CEST data was analysed only from a restricted set of residues for which | ϖ_{FU}| < 5ppm, the χ^2_{red} versus p_U plot does not contain a convincing minimum. Here we show that the analysis of the ^{15}N CEST data along with experimentally derived restraints on the folded state intrinsic (exchange-free) transverse relaxation rate ($R_{2,F}$) and visible state peak-positions (ϖ_{Vis}) resulted in sharper and more pronounced minima in the χ^2_{red} versus p_U and χ^2_{red} versus $k_{ex,FU}$ plots even when only residues with | ϖ_{FU}| < 5ppm (| ω_{FU}| < ~2230 rad/s at 700 MHz) were analysed showing that ^{15}N CEST data supplemented with experimentally derived restraints can be used to study relatively fast processes with k_{ex}/| ω| ~5. The folding kinetics and thermodynamics of PSBD were studied as a function of temperature (33.2 to 42.9 °C). As with other fast folding proteins the folding rate of PSBD is essentially invariant with temperature while the unfolding rate increases with temperature. An Arrhenius analysis of the temperature dependent rates suggests that PSBD folds over a small barrier involving a transition state that is more ordered and contains more energetically favourable interactions than the U state.

Materials and methods

Sample details

U-[^{15}N] PSBD was expressed in BL21(DE3) *E. coli* cells and purified as described previously (Gopalan and Vallurupalli, 2018). The 550 μl sample contained ~2 mM protein in a 20 mM sodium acetate, 50 mM NaCl, 1 mM NaN$_3$, 1 mM EDTA, 10% D$_2$O, pH 5.5 buffer.

NMR Experiments

The NMR experiments were carried out on Bruker Avance III HD (700 MHz) and Avance Neo (500 MHz) spectrometers. The 700 MHz spectrometer was equipped with a

cryogenically cooled triple resonance probe while the 500 MHz spectrometer was equipped with a room temperature probe.

All the CEST experiments were performed at 700 MHz using the ^{15}N CEST pulse sequence (Vallurupalli, Bouvignies, and Kay, 2012) in which the amide proton is decoupled from the amide ^{15}N nucleus using $90_x240_y90_x$ inversion pulses (Levitt, 1982). At 42.9 °C, four CEST datasets were recorded using B_1 (T_{EX}; offset range) values of 53.6 (450 ms; ±1400 Hz), 107.2 (375 ms; ±1900 Hz), 200.3 (350 ms; ; ±1900 Hz) and 300.5 (300 ms; ±1900 Hz) Hz with the ^{15}N carrier at 119.416 ppm. The spacing between adjacent B_1 offsets was 50 Hz for all four values of B_1. Each two-dimensional ^{15}N-^{1}H^N correlation map was recorded with 18 complex points (sweep width of 1845 Hz) in the indirect dimension and four transients per FID leading to an acquisition time ~6 minutes per plane. The strength of the ^{15}N B_1 field applied during the T_{EX} period was calibrated using the nutation method suggested by Guenneugues et al (Guenneugues, Berthault, and Desvaux, 1999). Very similar experimental parameters were used to record ^{15}N CEST data at the other four temperatures (33.2, 35.5, 38.3 and 40.3 °C).

The transverse ^{15}N-^{1}H^N dipole-dipole/^{15}N CSA interference rate constants (η_{xy}) at different backbone amide sites in PSBD were obtained at 700 MHz (33.2, 35.5, 38.3, 40.3 and 42.9 °C) by measuring the decays (Bouguet-Bonnet, Mutzenhardt, and Canet, 2004) of the amide ^{15}N TROSY and anti-TROSY components (Pervushin et al., 1997). Relaxation delays varied from 0 to 30 ms in steps of 5 ms with two repeats for error estimation. ^{15}N TROSY and anti-TROSY decays were recorded in an interleaved manner in ~9 hours. Intrinsic transverse relaxation rates (R_2) were obtained from the (^{15}N-^{1}H^N) dipole-dipole/ (^{15}N) CSA relaxation interference rate constant η_{xy} using the relation $R_2 = k\eta_{xy}$, with $\kappa = \sqrt{3}\frac{(4c^2 + 3d^2)}{12cdP_2(\cos\beta)}$ (Fushman, Tjandra, and Cowburn, 1998; Wang and Palmer, 2003). Here $c = \frac{\gamma_N B_0 \Delta \sigma}{\sqrt{3}}, d = \frac{-\mu_0 h\gamma_H\gamma_N}{8\pi^2 r_{NH}^3}$, h is the Planck's constant, μ_0 the permittivity of free space, r_{NH} (=1.02 Å) is the N-H bond length, B_0 is the external magnetic field, σ (= -173 ppm) is the chemical shift anisotropy of the ^{15}N site, β (=19.6°) is the angle between the N-H bond vector and the symmetry axis of the ^{15}N chemical shift tensor while γ_H and γ_N are the gyromagnetic ratios of the ^{1}H and ^{15}N nuclei respectively.

High-resolution amide ^{15}N-^{1}H^N HSQC spectra to obtain the visible state peak positions (ϖ_{Vis}) in the ^{15}N dimension were recorded at 700 MHz (33.2, 35.5, 38.3, 40.3 and 42.9 °C) using the experiment proposed by Skrynnikov et al. (Skrynnikov, Dahlquist, and Kay, 2002). The maximum evolution time in the indirect ^{15}N dimension was 60 ms. Two ^{15}N-^{1}H^N correlation maps were recorded at each temperature to estimate uncertainties in the peak positions. Each ^{15}N-^{1}H^N correlation map was recorded in three hours.

^{15}N and ^{1}H^N CPMG experiments (Gopalan, Hansen, and Vallurupalli, 2018) were carried out only at 42.9 °C at both 500 and 700 MHz. Amide ^{15}N CPMG relaxation-dispersion data was recorded using a constant-time (Mulder et al., 2001) ^{15}N TROSY-CPMG sequence (Loria, Rance, and Palmer, 1999b; Vallurupalli et al., 2007) with T_{EX} delays of 30 (500 MHz) and 20 (700 MHz) ms. Data was recorded for $\nu CPMG$ values varying from 66.66

Hz (500 MHz)/100 Hz (700 MHz) to 1000 Hz. Amide $^1H^N$ CPMG data was recorded using a constant-time sequence (Ishima and Torchia, 2003) without a P-Element (Vallurupalli, Bouvignies, and Kay, 2011; Yuwen and Kay, 2019). T_{EX} was set to 20 ms with $\nu CPMG$ varying from 100 Hz to 3000 Hz. To obtain a relaxation dispersion curve, $^{15}N/(^1H^N)$ CPMG data was recorded at several (10-20) different ν_{CPMG} values with errors estimated based on a few repeat (2-5) measurements.

Data analysis

The NMRPipe suite of programs (Delaglio et al., 1995) was used for processing all the NMR data and SPARKY (Goddard and Kneller, 2008; Lee, Tonelli, and Markley, 2015) was used for visualization and to obtain peak centres. The software package PINT (Ahlner et al., 2013) was used to quantify the peak intensities in the various CEST/CPMG ^{15}N-$^1H^N$ correlation maps.

The *ChemEx* package (Bouvignies, 2012) that numerically integrates (Korzhnev et al., 2004) the Bloch-McConnell equations (McConnell, 1958) was used to estimate various global exchange ($k_{ex,FU}$, p_U) and residue specific parameters (ϖ_F, ϖ_U, $R_{1,F}$ and $R_{2,F}$) from the data by minimising a standard $\chi^2 = \sum_{i=1}^{N} \frac{(m_i^{Calc} - m_i^{Exp})^2}{\sigma_i^2}$ function. Here m_i^{Exp} is the experimental measure (i.e. peak intensity in the case of CPMG/CEST datasets or peak position in the case of the HSQC datasets), m_i^{Calc} is the value calculated using the Bloch-McConnell equations and σ_i is the uncertainty in the experimentally measured value. The summation extends over all the experimental data used during the fitting process. Minimum uncertainties of 0.4% and 3 ppb were assumed for the ^{15}N CEST intensities and visible peak positions (ϖ_{Vis}) respectively. The two-state (F$\rightleftharpoons$U) Bloch-McConnell equations were constructed assuming $R_{2,U} = R_{2,F}/2$ and $R_{1,U} = R_{1,F}$ via previously published procedures (Korzhnev et al., 2004; Vallurupalli, Bouvignies, and Kay, 2012). Here $R_{2,U}$ was constrained to be $R_{2,F}/2$ (Farrow et al., 1995) as a different dip is not observed for the U state in the CEST intensity profiles (Tiwari et al., 2021). Intensities in the case of the CEST/CPMG experiments were calculated by numerically integrating the Bloch-McConnell equations for the duration of the T_{EX} period (Korzhnev et al., 2004; Vallurupalli, Bouvignies, and Kay, 2012). Visible peak-positions (ϖ_{Vis}) were calculated from the eigenvalues of the Bloch-McConnell equations (Anet and Basus, 1978; Skrynnikov, Dahlquist, and Kay, 2002). Uncertainties in the ^{15}N CEST intensities were estimated from the scatter in the flat parts of the intensity profile (Vallurupalli, Bouvignies, and Kay, 2012). Due to the broad dip sizes in the ^{15}N CEST intensity profiles, only the $B_1 \sim 50$ Hz profiles contained flat portions. Hence uncertainties were estimated only from the $B_1 \sim 50$ Hz profiles and these same values were used to analyse the CEST profiles recorded with higher B_1 values.

^{15}N CEST data from a select set (Set 1) of 18 residues was analysed globally (common $k_{ex,FU}$ and p_U). These 18 residues (I3, A4, V8, R9, A12, R13, K15, D18, I19, R20, L21, Q23, G24, G29, V31, D37, L40 and L41) had CEST derived ^{15}N | ϖ_{FU}| values 3 ppm at 42.9 °C. The same set of 18 residues was used for the global analysis of ^{15}N CPMG data at 42.9 °C and ^{15}N CEST data at all the other temperatures. $^1H^N$ CPMG data from 12 residues (I3, M5, V8, R13, K15, G16, V22, Q23, R30, K33, I36, D37) for which $R_{2,eff}$ (100 Hz) –

$R_{2,eff}$ (3000 Hz) 5 s^{-1} at both 500 and 700 MHz was analysed globally using a two-state exchange model. Residue specific ϖ_{FU} values for the other sites (other than Fig 1) were obtained by fixing the $k_{ex,FU}$ and p_U values to those obtained from the global analysis of the above specified subset(s) of residues. In some cases the analysis was performed on a smaller set (Set 2) of 14 residues (I3, A4, V8, R9, R13, D18, R20, Q23, G24, G29, V31, D37, L40 and L41) that had CEST derived ^{15}N | ϖ_{FU}| values between 3 and 5 ppm at 42.9 °C. Uncertainties in the best-fit exchange parameters were obtained using a standard bootstrap procedure (Choy et al., 2005; Press et al., 1992) with 250 trials.

Kinetic and thermodynamic parameters (ΔH^*_{UF}, ΔS^*_{UF}, H_{UF} and S_{UF}) for the PSBD folding process were obtained by analysing the temperature dependence of the folding (k_{UF}) and unfolding (k_{FU}) rate constants as described previously (Vallurupalli et al., 2016) using modified Kramers-Arrhenius equations, $k_{UF}(T) = \frac{k_0}{\eta(T)/\eta_0}e^{-\frac{(\Delta H^*_{UF} - T\Delta S^*_{UF})}{RT}}$ and

$k_{FU}(T) = \frac{k_0}{\eta(T)/\eta_0}e^{-\frac{(\Delta H^*_{UF} - \Delta H_{UF} - T(\Delta S^*_{UF} - \Delta S_{UF}))}{RT}}$ (Ansari et al., 1992; Hagen, 2010; Sekhar, Vallurupalli, and Kay, 2012). ΔH^*_{UF} and ΔS^*_{UF} are respectively the activation enthalpy and activation entropy for the folding reaction. H_{UF} and S_{UF} are respectively the change in enthalpy and entropy upon folding. R is the universal gas constant, $\eta(T)$ is the viscosity at temperature T, while η_0 is (1 cP) the viscosity of water at a reference temperature of 293.15 K. k_0 was set to 2.27×10^6 s^{-1} (at all temperatures) according to the formula suggested by Eaton (Eaton, 2021) for the folding speed-limit of a 44 residue protein. A Monte Carlo procedure (Press et al., 1992) with 100 trials was used to estimate the uncertainties in the estimates of ΔH^*_{UF}, ΔS^*_{UF}, H_{UF} and S_{UF}.

Results and Discussion

^{15}N CEST detects exchange occurring on the 100 µs timescale

The 44 residue PSBD from the pyruvate dehydrogenase multienzyme complex of *Bacillus stearothermophilus* is a largely helical protein (Allen et al., 2005) that folds on the ~10-100 µs timescale (Fig 1a). PSBD has served as a model system to understand protein folding and its folding has been extensively investigated by several techniques (Ferguson et al., 2005; Spector and Raleigh, 1999; Vugmeyster et al., 2000). At 42.9 °C the amide ^{15}N-^{1}H^N correlation map is well resolved containing peaks arising from the native folded state (Fig 1b). The ^{15}N CEST profiles recorded using a U-[^{15}N] PSBD sample contained a single dip near the visible state resonances (Fig 1c). However a model in which only the native state is populated at 42.9 °C did not account ($\chi^2_{red} = 2$) for the ^{15}N CEST profiles (B_1 values of 53.6, 107.2, 200.3 and 300.5 Hz) obtained from 33 different residues. The ^{15}N CEST profiles were however accounted for ($\chi^2_{red} = 0.77$) by a global two-state exchange model in which the folded (F) state exchanges with an 'invisible' unfolded state (U) with best-fit $p_U = 3.9\%$ and $k_{ex,FU} = 11363$ s^{-1}. There are large changes in chemical shift between major state and the minor state along the sequence (Fig. 1d) and the minor state chemical shifts obtained from the analysis of the CEST data are in very good agreement (Fig. 1e, rmsd 0.91 ppm) with predicted U state shifts (Nielsen and Mulder, 2018) confirming that the minor state is indeed

the unfolded state. In the discussion that follows the F state will refer to the major state and the U state to the minor state.

To test if the exchange parameters obtained from the analysis of the ^{15}N CEST data are reliable we analysed data from a select set of 18 residues for which $|\varpi_{FU}|$ 3 ppm (see materials and methods). As before the two-state model accounted for the ^{15}N CEST data (χ^2_{red} = 0.76) and although reasonably precise estimates of p_U (4.0 ± 0.32%) and $k_{ex,FU}$ (11317 ± 376) s^{-1} were obtained, the χ^2_{red} versus $k_{ex,FU}$ and χ^2_{red} versus p_U plots (black line in Fig 2a,b) are quite flat. In our experience these shallow or non-existent minima can lead to spurious "precise" solutions due to some unaccounted artifacts/features in the data that the model attempts to satisfy. Consequently to rule out spurious solutions and determine reliable exchange parameters it is important to obtain more pronounced global minima in the χ^2_{red} versus $k_{ex,FU}$ and χ^2_{red} versus p_U plots. This can be achieved by constraining the fitting parameters to reasonable values (Palmer and Koss, 2019) or by judiciously including in the fitting procedure additional experimental data that complements the existing data (Bouvignies et al., 2011; Farber, Slager, and Mittermaier, 2012; Gopalan and Vallurupalli, 2018; Igumenova et al., 2007; Korzhnev et al., 2005; Mulder et al., 1999; Neudecker, Korzhnev, and Kay, 2006; Vallurupalli, Bouvignies, and Kay, 2011).

Constraints on the major-state transverse relaxation rates leads to more reliable exchange parameters

The best-fit procedure to obtain exchange parameters from the ^{15}N CEST data optimises residue specific parameters ϖ_F, ϖ_U, $R_{1,F}$ and $R_{2,F}$ in addition to the global exchange parameters ($k_{ex,FU}$ and p_U). Here $R_{1,i}$ and $R_{2,i}$ respectively refer to the longitudinal and intrinsic transverse relaxation rates of the spin of interest in state i ($i \in$ F,U). To test if any of the residue-specific parameters might be compensating for improper $k_{ex,FU}$ and p_U values, we examined how the best-fit residue-specific parameters varied as a function of $k_{ex,FU}$ and p_U (Fig S1). (In these fits, constraints $R_{2,F}$ 0 s^{-1} and $R_{2,U} = R_{2,F}/2$ were imposed.) For the ~4.7 kDa PSBD, we expect the amide ^{15}N $R_{2,F}$ to be around ~3 to 4 s^{-1} at 42.9 °C. However plots of the best-fit $R_{2,F}$ values versus $k_{ex,FU}$ (Fig S1a) and p_U (Fig S1b) show that the fitted $R_{2,F}$ values vary significantly as a function of $k_{ex,FU}$ and p_U. They can be very large (> 8 s^{-1}) when $k_{ex,FU}$ and p_U are smaller than the 'right' values (grey line Fig S1a) and very small (~0 s^{-1}) when $k_{ex,FU}$ and p_U are greater than the 'right' values. (For the discussion here, $k_{ex,FU}$ = 11739 s^{-1} and p_U = 4.3% obtained later using more data and restraints [Table 1] are considered to be the 'right' exchange parameters.) To try and rationalise these trends in the fitted $R_{2,F}$ values, we tried to understand how various parameters affect the shape of the CEST intensity profile that can be approximated (Palmer, 2014; Palmer and Koss, 2019) as:

$$I/I_0 \approx \cos^2\theta e^{-R_{1\rho}T_{EX}}$$

(1)

with

$$R_{1\rho}(\omega_1, \omega_{RF}) = R_1\cos^2\theta + (R_2 + R_{ex}(\omega_1, \omega_{RF}))\sin^2\theta$$

(2)

For simplicity here we have assumed that both states have the same longitudinal (R_1) and intrinsic transverse (R_2) relaxation rates. Then the exchange contribution to the transverse relaxation (R_{ex}) of the visible state can be approximated as (Palmer, 2014; Palmer and Koss, 2019; Trott and Palmer, 2002):

$$R_{ex}(\omega_1, \omega_{RF}) \approx \frac{p_F p_U \, \Delta \, \omega_{FU}^2}{k_{ex,FU}} \left[\frac{k_{ex,FU}^2}{k_{ex,FU}^2 + \frac{\omega_{F,eff}^2 \omega_{U,eff}^2}{\omega_{eff}^2}} \right]$$

(3)

Here $\omega_{i,eff}^2 = (\Omega_i^2 + \omega_1^2)$, $\omega_1 = 2\pi B_1$, $\Omega_i = \omega_i - \omega_{RF}$ is the offset (rad/s) of the nucleus of interest in state i ($i \in$ F,U) from the frequency (ω_{RF}) at which the B_1 field is applied, $\omega_{eff}^2 = (\overline{\Omega}^2 + \omega_1^2)$ with $\overline{\Omega} = p_F \omega_F + p_U \omega_U - \omega_{RF}$ and $\tan\theta = \omega_1/\overline{\Omega}$.

It is clear from equation 3 that R_{ex} depends on the strength of B_1 field, the offset (ω_{RF}) at which it is applied, exchange parameters ($k_{ex,FU}$, p_U) and the resonance frequencies of the spin of interest in the major (ω_F) and minor (ω_U) states. Hence mis-setting $k_{ex,FU}$ or p_U can lead to erroneous R_{ex} values that can be compensated for by adjusting the value of R_2 (Equation 2) in a way that the shape of the CEST intensity profile remains nearly the same (Vugmeyster et al., 2000). Thus, constraining the R_2 rates to their correct values can lead to more accurate estimates of the best-fit exchange parameters. R_1 on the other hand is well defined from the flat parts of the CEST profiles. It is useful to note that in the case of slow-exchange unlike the case of intermediate/fast exchange being studied here, the CEST intensity profile will contain separate (relatively narrow) dips for the major and minor states and accurate intrinsic transverse relaxation rates for the two states can be obtained from the analysis of the CEST data (Vallurupalli, Bouvignies, and Kay, 2012) and there may be no need to additionally constrain them. In fact CEST experiments have been used to measure intrinsic R_2 rates both in the absence (Bain, Ho, and Martin, 1981) and presence (Gu et al., 2016) of exchange. In the case of fast exchange for reasons similar to those discussed above, R_2 rates have been constrained while analyzing CPMG (O'Connell et al., 2009) and $R_{1\rho}$ (Vugmeyster et al., 2000) data. The potential power of R_2 constraints in the context of CEST experiments was recently illustrated in a study of the folding of the A39G FF domain using ^{15}N CEST experiments at 600 and 1000 MHz. The R_2 values of the minor states were linked to the R_2 values of the major state (that were fit) and this resulted in the detection of exchange occurring at ~8,500 s^{-1} between two minor states populated to just ~1% and ~0.34% respectively in a four state system (Tiwari et al., 2021). Here we are proposing doing the same for the major state to study rapid exchange between the major and a minor state.

The transverse relaxation rate of the ^{15}N nucleus in an amide ^{15}N-^{1}H^N spin-system is dominated by its chemical-shift anisotropy (CSA) and the dipole-dipole interaction with the attached proton and reasonably accurate estimates of the intrinsic (exchange free) ^{15}N R_2 values can be very conveniently obtained from the transverse (^{15}N-^{1}H^N) dipole-dipole/(^{15}N)

CSA relaxation interference rate constant (η_{xy}) that is insensitive to exchange (Fushman, Tjandra, and Cowburn, 1998; Wang and Palmer, 2003). Other approaches have also been proposed to obtain the exchange free intrinsic transverse relaxation rates of the visible state (Hansen et al., 2007; Phan, Boyd, and Campbell, 1996). Here we have confirmed that the ^{15}N R_2 values obtained from η_{xy} values are in reasonable agreement (~±10%, maximum deviation of ~30%) with those obtained from ^{15}N CEST data by carrying out measurements on ^{15}N enriched samples of T4 lysozyme (Fig. S2). Next we obtained estimates of the $R_{2,F}$ values from η_{xy} measurements on the PSBD sample at 42.9 °C (Fig. S3) and constrained the fitted $R_{2,F}$ values to be within±50% of the estimates obtained from the η_{xy} measurements. The constraints did not alter the quality of the fits ($\chi^2_{red} = 0.77$) but lead to slightly more precise estimates of exchange parameters, $p_U = 4.43 \pm 0.20\%$ and $k_{ex,FU} = 11688 \pm 142$ s^{-1}. The χ^2_{red} versus $k_{ex,FU}$ and χ^2_{red} versus p_U plots with the constraints on $R_{2,F}$ values are shown using blue lines in figures 2a and 2b respectively. It is clear from the χ^2_{red} versus $k_{ex,FU}$ plot that constraints on the $R_{2,F}$ values does not allow for solutions (compare the blue and black lines in Fig. 2a) with low $k_{ex,FU}$ values leading to a clear minimum at ~11,688 s^{-1}. Constraints on the $R_{2,F}$ values also rule out solutions (compare the blue and black lines in Fig. 2b) with low p_U values but still allow for solutions with large p_U values. Thus unlike in the χ^2_{red} versus $k_{ex,FU}$ plot we still do not have a clear minimum in the χ^2_{red} versus p_U plot.

Visible state peak-positions can also lead to more reliable exchange parameters

When exchange is fast ($k_{ex,FU} \gg |\varpi_{FU}|$), it is difficult to get independent estimates of the minor state population (p_U) and the chemical shift difference (ϖ_{FU}) from relaxation data as they can be varied in a correlated manner to reproduce the measured relaxation rates (Luz and Meiboom, 1963; Palmer, 2004). This is evident from equation 3 which shows that changes in p_U can be compensated by adjusting ω_{FU} such that $p_F p_U \Delta \omega^2_{FU}$ remains constant. It is clear from Figure S1c that large p_U values are accommodated by the ^{15}N CEST data here (Fig 1b blue line) by scaling ω_{FU} such that $p_F p_U \Delta \omega^2_{FU}$(or $p_F p_U \Delta \varpi^2_{FU}$) remains largely constant. To break this correlation between p_U and ω_{FU} we need to include in the fitting procedure experimental data that has a different dependence on p_U and ω_{FU}. The exchange induced shift (δ_{ex}; rad/s) of the dominant visible state peak is one such parameter (Palmer, 2004; Vallurupalli, Bouvignies, and Kay, 2011). When $p_U \ll 1$ we have (Palmer, 2004; Swift and Connick, 1962; Vallurupalli, Bouvignies, and Kay, 2011):

$$\delta_{ex} = \frac{p_U \Delta \omega_{FU}}{1 + (\frac{\Delta \omega_{FU}}{k_{ex,FU}})^2}$$

(4)

Hence when $k_{ex,FU} \gg |\varpi_{FU}|$ equation 4 simplifies to:

$$\delta_{ex} \approx p_U \Delta \omega_{FU}\left(1 - \left(\frac{\Delta \omega_{FU}}{k_{ex,FU}}\right)^2\right)$$

(5)

It is clear from equations 3 and 5, that R_{ex} and δ_{ex} have different dependencies on p_U and ω_{FU} in the fast exchange limit (and $p_U \ll 1$). As $R_{ex} \propto p_U \Delta \omega_{FU}^2$ and $\delta_{ex} \propto p_U \omega_{FU}$ it will not be possible to compensate for incorrect p_U values by scaling ω_{FU} to obtain the correct R_{ex} and δ_{ex} values simultaneously. δ_{ex} cannot be directly measured, but the visible peak position $\omega_{Vis} = \omega_F + \delta_{ex}$ can be measured very accurately from ${}^1H^N$-${}^{15}N$ correlation maps. In figure 2c, root mean square deviation between the experimental visible state peak position in ppm (ϖ_{Vis}) and visible state peak position calculated ($\varpi_{Vis,calc}$) from parameters obtained from the best-fit procedure that included experimentally derived constraints on the fitted $R_{2,F}$ values is shown for different p_U values. When $p_U \sim 4\%$ the deviation between the calculated and measured values is less than 30 ppb (~2 Hz at 700 MHz) but increases to more than 60 ppb when p_U in increased to 10% (Fig 2c). From equations 1–3 it is clear that the shape of the CEST intensity profile is a complicated function various exchange parameters and should contain information regarding ϖ_{Vis} which is probably why the ϖ_{Vis} values can be predicted reasonably well (~30 ppb) from the CEST derived best-fit parameters. However better estimates of ϖ_{Vis} values will probably not be available from the CEST data alone as the dips are on the order of a (few) ppm wide (Fig 1c). As ϖ_{Vis} can be measured very precisely (< 3 ppb) from ${}^{15}N$-${}^1H^N$ correlation maps, a combined analysis of experimentally measured ${}^{15}N$ ϖ_{Vis} values along with ${}^{15}N$ CEST data could make spurious solutions with large p_U values unlikely. Including the visible state peak-positions in fitting process along with the constraints on the $R_{2,F}$ values does not alter the quality of the fits ($\chi_{red}^2 = 0.78$) or the estimates of exchange parameters, $p_U = 4.3 \pm 0.17\%$ and $k_{ex,FU} = 11739 \pm 147$ s^{-1} but leads to a pronounced minimum in the χ_{red}^2 versus p_U plot as two-state solutions with higher p_U values can no longer satisfy the data (Fig 2b; red line). Including just the visible peak positions without constraints on the $R_{2,F}$ values during the fitting processes also rules out solutions with large p_U values (compare the green and blue lines in Fig 2b). Consistent with our earlier speculation that the high precision of the measured ϖ_{Vis} values is critical to improving the shape of the χ_{red}^2 versus p_U plot, we find that the well defined minimum starts to vanish when the uncertainty in the ϖ_{Vis} values is artificially increased from 3 to 30 ppb (Fig 2d). Even though the ϖ_{Vis} values do not lead to a quantitative improvement here, they rule out solutions with large p_U values confirming that the well-defined best-fit exchange parameters obtained without any constraints accurately reflect the kinetics in the sample and did not arise due to some artefacts in the data. It is worth noting that information from ϖ_{Vis} values is often implicitly included while analysing CEST data. This is done by either insisting that the major-state resonance is at ϖ_{Vis} in the case of slow exchange or that the population weighted chemical shift is at ϖ_{Vis} in the case of fast-exchange (Rangadurai, Shi, and Al-Hashimi, 2020; Vallurupalli, Bouvignies, and Kay, 2012).

To test if the p_U and $k_{ex,FU}$ parameters determined from the above analysis of the ${}^{15}N$ CEST data are accurate, we compared them to exchange parameters obtained from ${}^1H^N$ and ${}^{15}N$ CPMG data (Fig 3a,b) recorded on the same sample at 500 and 700 MHz. The CPMG data is consistent with a two-state exchange processes ($\chi_{red}^2 = 0.83$) and the χ_{red}^2 versus $k_{ex,FU}$ plot obtained from the analysis of the CPMG data has a clear minimum with a best-fit $k_{ex,FU} = 10987 \pm 275$ s^{-1} in reasonable agreement with the CEST derived value of 11739 ± 147 s^{-1} (Fig 3c). Based on previous ${}^1H^N$ and ${}^{15}N$ CPMG studies of PSBD folding (Gopalan

and Vallurupalli, 2018; Gopalan et al., 2018) we did not expect to obtain estimates of p_U from the $^1H^N$ and ^{15}N CPMG data alone as the system is in fast exchange which means that exchange models with incorrect (larger) p_U values can fit the data by scaling the fitted ϖ_{FU} values by $\sqrt{p_{U, Correct}/p_{U, Fitted}}$ (Gopalan and Vallurupalli, 2018; Luz and Meiboom, 1963; Vallurupalli, Bouvignies, and Kay, 2011). Here $p_{U,correct}$ and $p_{U,Fitted}$ refer to the correct and fitted p_U values respectively. Hence if the CEST derived p_U value is correct there should be a good correlation with a slope of ~1 between the CPMG derived ϖ_{FU} values with p_U fixed to the CEST derived value of 4.3% and those reported previously by simultaneously analysing $^1H^N$, ^{15}N, methyl ^1H TQ CPMG data along with $^1H^N/^{15}N$ H(S/M)QC & methyl ^1H SQ/DQ/TQ shift data (Vallurupalli, Bouvignies, and Kay, 2011; Yuwen, Vallurupalli, and Kay, 2016). As expected the χ^2_{red} versus p_U plot obtained from an analysis of the $^1H^N$ and ^{15}N CPMG data does not contain a pronounced minimum (Fig 3d). However, there is a small minimum at $p_U = 2.21\%$, that turns out to be a spurious minimum of the kind that we are worried about. When the $^1H^N$ & ^{15}N CPMG data was analysed with p_U set to the ^{15}N CEST derived value of 4.3% the slope between the CPMG derived $^1H^N$ | ϖ_{FU}| and ^{15}N ϖ_{FU} values and the previously reported $^1H^N$ | ϖ_{FU}| and ^{15}N ϖ_{FU} values is 0.92 (Fig 3e) showing that the p_U of 4.3% obtained from the ^{15}N CEST data is correct ($0.92^2 \approx 0.85$) to within 20%, assuming that the previously reported ϖ_{FU} values are accurate. On the other hand there is a slope of 0.69 between the CPMG derived $^1H^N$ | ϖ_{FU}| and ^{15}N ϖ_{FU} values with $p_U = 2.21\%$ and the previously reported ϖ_{FU} values (Fig 3f) showing that the CPMG derived p_U of 2.21% is about half ($0.69^2 = 0.48 \approx (\frac{2.21\%}{4.3\%})$) of the 'correct' value confirming that the CPMG derived p_U of 2.21% is inaccurate and arises from a spurious minimum.

The effect of including R_2 constraints and ϖ_{Vis} values during the analysis of ^{15}N CEST data becomes even more apparent (Fig 4a,b) when we restrict the analysis to a select set of 14 residues (Set 2) that have | ϖ_{FU}| values between 3 and 5 ppm (Fig 4). Without any restraints $p_U = 3.61 \pm 0.38\%$ and $k_{ex,FU} = 11189 \pm 421$ adopt (Fig 4c,d,e) a slightly wide-range of values in 250 boot-strap trials (Fig 4e), but are a little better defined ($p_U = 4.14 \pm 0.22\%$ and $k_{ex,FU} = 11788 \pm 194$) with the restraints (Fig 4). Here too leaving out the ϖ_{Vis} values during the fitting process does not affect the precision of the exchange parameters ($p_U = 4.19 \pm 0.21\%$ and $k_{ex,FU} = 11654 \pm 179$ s^{-1}) but a clear minimum appears in the χ^2_{red} versus p_U plot only when the ϖ_{Vis} values are included in the fitting process (Fig 4b) showing that a convincing minimum can appear in χ^2_{red} versus p_U or the χ^2_{red} versus $k_{ex,FU}$ plots even in the case of relatively fast exchange, $k_{ex,FU}/|\omega_{FU}|$ ~5.

Kinetics and Thermodynamics of PSBD folding

To obtain insights into the rapid folding of PSBD under the conditions used here, we performed amide ^{15}N CEST experiments, η_{xy} and ϖ_{Vis} measurements at four additional temperatures 33.2, 35.5, 38.3, and 40.3 °C and analysed them using two-state (F$\rightleftharpoons$U) exchange model as described above to obtain exchange parameters at these additional temperatures (Table 1). We find that $k_{ex,FU}$ is not temperature dependent (Fig 5a) while p_U increases with temperature (Fig 5b, c) which means that the folding rate constant (k_{UF}) is largely independent of temperature while the unfolding rate constant (k_{FU}) increases with temperature (Fig 5d). Such behaviour has been observed for several fast-folding proteins

including PSBD (Bahar, Jernigan, and Dill, 2017; Spector and Raleigh, 1999) and predicted by the Zwanzig, Szabo, Bagchi (ZSB) model for protein folding (Zwanzig, 1995; Zwanzig, Szabo, and Bagchi, 1992). An Arrhenius analysis of rates leads to H_{FU} = 148.5 ± 9.7 kJ/mol, S_{FU} = 444 ± 31 J/mol·K, Δ H^*_{FU} = 143.6 ± 9.7kJ/mol and Δ S^*_{FU} = 380.6 ± 30.9J/mol · K (Fig 5c, d, e). Here H_{FU} and S_{FU} are differences in the enthalpy and entropy between the U and F states respectively. Δ H^*_{FU} and ΔS^*_{FU} are respectively the activation enthalpy and entropy for the FU process leading to activation parameters Δ H^*_{UF} = − 4.9 ± 2.4kJ/mol and Δ S^*_{UF} = − 63.8 ± 7.6J/mol · K for the folding (UF) process. While the activation free energy Δ G^*_{FU} for the unfolding process is 23.3 kJ/mol (8.9 *RT)* at 316.05 K, the activation free energy for the folding process Δ G^*_{UF} is a modest 15.2 kJ/mol (5.8 *RT*). Hence as the transition (T) state is only slightly more unstable (higher *G*) than the U state and PSBD is able to fold rapidly because the folding barrier is small (5.8 *RT*). Compared to the U state, the T state is is more ordered (-ve Δ S^*_{UF}) and also has favourable interactions (-ve Δ H^*_{UF}) but the favourable interactions do not overcome (Δ G^*_{UF} > 0) the loss of entropy due to ordering leading to the small folding barrier in line with the ZSB model (Zwanzig, 1995; Zwanzig, Szabo, and Bagchi, 1992).

Concluding Remarks

Here we have shown that imposing experimentally derived constraints on the major-state transverse relaxation rate and including the visible-state peak position during the analysis of amide ^{15}N CEST data acquired with very modest B_1 fields (~50 to ~300 Hz) results in reliable and more precise estimates of exchange parameters even when exchange rates are on the order of 10,000 s^{-1} that lies in the fast exchange limit with k_{ex}/| ω| values of ~5 (here for Set 2). Relatively fast processes can also be studied using a combination of amide ^{1}H^N/^{15}N CPMG experiments in combination with H(S/M)QC shifts (Vallurupalli, Bouvignies, and Kay, 2011). Even though ^{15}N CEST and ^{1}H^N/^{15}N CPMG & H(S/M)QC data are recorded from the same amide sites, large (useful) shift differences between ^{15}N-^{1}H^N HSQC and HMQC spectra are observed only for sites where ^{1}H^N and ^{15}N | ω| values are large and similar, reducing the efficacy of this strategy compared to the ^{15}N CEST based strategy that works so long as the ^{15}N | ω| values are large. Very fast exchange (~25,000 s^{-1}) can also be studied using amide ^{15}N E-CPMG and high-power $R_{1,\rho}$ experiments but they do not directly provide estimates of the minor state populations and chemical shifts (Ban et al., 2012; Reddy et al., 2018). These various approaches can in principle be combined with the ^{15}N CEST based strategy presented here to obtain more accurate estimates of the exchange parameters. Calculations (Fig. S4) also suggest that the strategy presented here of constraining $R_{2,F}$ values along with the inclusion of accurate ϖ$_{Vis}$ shifts while analysing ^{15}N CEST data will work for medium sized proteins ($R_{2,F}$= 15 s^{-1}, ~15 kDa at 25 °C). It may be possible to extend the strategies presented here in the context of the amide ^{15}N-^{1}H^N system to study exchange at various ^{13}C sites in proteins using site-specifically ^{13}C enriched samples (Goto et al., 1999; Hansen et al., 2008; Lundstrom, Lin, and Kay, 2009; Lundstrom et al., 2007; Lundstrom et al., 2009) that are free from the deleterious effects of carbon-carbon J couplings (Bouvignies, Vallurupalli, and Kay, 2014; Vallurupalli, Bouvignies, and Kay, 2013; Zhou and Yang, 2014).

As the utility of the amide ^{15}N CEST experiments to study protein dynamics occurring on the ~10^{-1} to ~10^{-2} second timescale is well established, the developments presented here show that proteins dynamics occurring over the entire ~10^{-1} to ~10^{-4} second timescale can be studied using simple amide ^{15}N CEST experiments performed on a single uniformly ^{15}N enriched sample.

Supplementary Material

Refer to Web version on PubMed Central for supplementary material.

Acknowledgements

References

Ahlner A, Carlsson M, Jonsson BH, Lundstrom P. PINT: a software for integration of peak volumes and extraction of relaxation rates. J Biomol NMR. 2013; 56: 191–202. [PubMed: 23657843]

Allen MD, Broadhurst RW, Solomon RG, Perham RN. Interaction of the E2 and E3 components of the pyruvate dehydrogenase multienzyme complex of Bacillus stearothermophilus. Use of a truncated protein domain in NMR spectroscopy. FEBS J. 2005; 272: 259–68. [PubMed: 15634348]

Allerhand A, Thiele E. Analysis of Carr—Purcell Spin-Echo NMR Experiments on Multiple-Spin Systems. II. The Effect of Chemical Exchange. Journal of Chemical Physics. 1966; 45: 902–916.

Anet FAL, Basus VJ. Limiting Equations for Exchange Broadening in 2-Site Nmr Systems with Very Unequal Populations. J Magn Reson. 1978; 32: 339–343.

Ansari A, Jones CM, Henry ER, Hofrichter J, Eaton WA. The role of solvent viscosity in the dynamics of protein conformational changes. Science. 1992; 256: 1796–8. [PubMed: 1615323]

Anthis NJ, Clore GM. Visualizing transient dark states by NMR spectroscopy. Q Rev Biophys. 2015; 48: 35–116. [PubMed: 25710841]

Avram L, Wishard AD, Gibb BC, Bar-Shir A. Quantifying Guest Exchange in Supramolecular Systems. Angew Chem Int Ed Engl. 2017; 56: 15314–15318. [PubMed: 28972281]

Bahar, I, Jernigan, R, Dill, KA. Garland Science. Taylor & Francis Group; New York: 2017.

Bain AD, Ho WPY, Martin JS. A New Way of Measuring NMR Spin-Spin Relaxation Times (T2). J Magn Reson. 1981; 43: 328–330.

Ban D, Gossert AD, Giller K, Becker S, Griesinger C, Lee D. Exceeding the limit of dynamics studies on biomolecules using high spin-lock field strengths with a cryogenically cooled probehead. J Magn Reson. 2012; 221: 1–4. [PubMed: 22743535]

Bolik-Coulon N, Hansen DF, Kay LE. Optimizing frequency sampling in CEST experiments. J Biomol NMR. 2022; 76: 167–183. [PubMed: 36192571]

Bouguet-Bonnet S, Mutzenhardt P, Canet D. Measurement of 15N csa/dipolar cross-correlation rates by means of Spin State Selective experiments. J Biomol NMR. 2004; 30: 133–42. [PubMed: 15666560]

Bouvignies G. Chemex. 2012. (https://github.com/gbouvignies/chemex/releases)

Bouvignies G, Hansen DF, Vallurupalli P, Kay LE. Divided-evolution-based pulse scheme for quantifying exchange processes in proteins: powerful complement to relaxation dispersion experiments. J Am Chem Soc. 2011; 133: 1935–45. [PubMed: 21244030]

Bouvignies G, Kay LE. A 2D C-13-CEST experiment for studying slowly exchanging protein systems using methyl probes: an application to protein folding. J Biomol NMR. 2012; 53: 303–310. [PubMed: 22689067]

Bouvignies G, Vallurupalli P, Kay LE. Visualizing Side Chains of Invisible Protein Conformers by Solution NMR. Journal of Molecular Biology. 2014; 426: 763–774. [PubMed: 24211467]

Cavanagh, J, Fairbrother, WJ, Palmer, AG, Rance, M, Skelton, NJ. Protein NMR Spectroscopy, Principles and Practice. 2nd ed. Academic Press; 2006.

Chao FA, Zhang Y, Byrd RA. Theoretical classification of exchange geometries from the perspective of NMR relaxation dispersion. J Magn Reson. 2021; 328 107003 [PubMed: 34058714]

Choy WY, Zhou Z, Bai Y, Kay LE. An 15N NMR spin relaxation dispersion study of the folding of a pair of engineered mutants of apocytochrome b562. J Am Chem Soc. 2005; 127: 5066–72. [PubMed: 15810841]

Delaglio F, Grzesiek S, Vuister GW, Zhu G, Pfeifer J, Bax A. NMRPipe - a Multidimensional Spectral Processing System Based on Unix Pipes. J Biomol NMR. 1995; 6: 277–293. [PubMed: 8520220]

Deshmukh L, Louis JM, Ghirlando R, Clore GM. Transient HIV-1 Gag-protease interactions revealed by paramagnetic NMR suggest origins of compensatory drug resistance mutations. Proceedings of the National Academy of Sciences of the United States of America. 2016; 113: 12456–12461. [PubMed: 27791180]

Eaton WA. Modern Kinetics and Mechanism of Protein Folding: A Retrospective. J Phys Chem B. 2021; 125: 3452–3467. [PubMed: 33724035]

Farber PJ, Slager J, Mittermaier AK. Local folding and misfolding in the PBX homeodomain from a three-state analysis of CPMG relaxation dispersion NMR data. J Phys Chem B. 2012; 116 10317-29 [PubMed: 22845760]

Farrow NA, Zhang O, Forman-Kay JD, Kay LE. Comparison of the backbone dynamics of a folded and an unfolded SH3 domain existing in equilibrium in aqueous buffer. Biochemistry. 1995; 34: 868–78. [PubMed: 7827045]

Fawzi NL, Ying J, Ghirlando R, Torchia DA, Clore GM. Atomic-resolution dynamics on the surface of amyloid-beta protofibrils probed by solution NMR. Nature. 2011; 480: 268–72. [PubMed: 22037310]

Ferguson N, Sharpe TD, Schartau PJ, Sato S, Allen MD, Johnson CM, Rutherford TJ, Fersht AR. Ultra-fast barrier-limited folding in the peripheral subunit-binding domain family. J Mol Biol. 2005; 353: 427–46. [PubMed: 16168437]

Forsen S, Hoffman RA. Study of Moderately Rapid Chemical Exchange Reactions by Means of Nuclear Magnetic Double Resonance. J Chem Phys. 1963; 39: 2892–2901.

Fushman D, Tjandra N, Cowburn D. Direct Measurement of 15N Chemical Shift Anisotropy in Solution. J Am Chem Soc. 1998; 120: 10947–10952.

Gladkova C, Schubert AF, Wagstaff JL, Pruneda JN, Freund SMV, Komander D. An invisible ubiquitin conformation is required for efficient phosphorylation by PINK1. EMBO J. 2017; 36: 3555–3572. [PubMed: 29133469]

Goddard, TD, Kneller, DG. SPARKY 3. University of California; San Francisco: 2008.

Goerke S, Milde KS, Bukowiecki R, Kunz P, Klika KD, Wiglenda T, Mogk A, Wanker EE, Bukau B, Ladd ME, Bachert P, et al. Aggregation-induced changes in the chemical exchange saturation transfer (CEST) signals of proteins. NMR Biomed. 2017; 30

Gopalan AB, Hansen DF, Vallurupalli P. CPMG Experiments for Protein Minor Conformer Structure Determination. Methods Mol Biol. 2018; 1688: 223–242. [PubMed: 29151212]

Gopalan AB, Vallurupalli P. Measuring the signs of the methyl ^{1}H chemical shift diferences between major and 'invisible' minor protein conformational states using methyl ^{1}H multi-quantum spectroscopy. J Biomol NMR. 2018; 70: 187–202. [PubMed: 29564579]

Gopalan AB, Yuwen T, Kay LE, Vallurupalli P. A methyl (1)H double quantum CPMG experiment to study protein conformational exchange. J Biomol NMR. 2018; 72: 79–91. [PubMed: 30276607]

Goto NK, Gardner KH, Mueller GA, Willis RC, Kay LE. A robust and cost-effective method for the production of Val, Leu, Ile (delta 1) methyl-protonated 15N-, 13C-, 2H-labeled proteins. J Biomol NMR. 1999; 13: 369–74. [PubMed: 10383198]

Gu YN, Hansen AL, Peng Y, Bruschweiler R. Rapid Determination of Fast Protein Dynamics from NMR Chemical Exchange Saturation Transfer Data. Angew Chem Int Edit. 2016; 55: 3117–3119.

Guenneugues M, Berthault P, Desvaux H. A method for determining B_1 field inhomogeneity. Are the biases assumed in heteronuclear relaxation experiments usually underestimated? J Magn Reson. 1999; 136: 118–26. [PubMed: 9887297]

Hagen SJ. Solvent viscosity and friction in protein folding dynamics. Curr Protein Pept Sci. 2010; 11: 385–95. [PubMed: 20426733]

Hansen DF, Vallurupalli P, Kay LE. Using relaxation dispersion NMR spectroscopy to determine structures of excited, invisible protein states. J Biomol NMR. 2008; 41: 113–20. [PubMed: 18574698]

Hansen DF, Vallurupalli P, Lundstrom P, Neudecker P, Kay LE. Probing chemical shifts of invisible states of proteins with relaxation dispersion NMR spectroscopy: how well can we do? J Am Chem Soc. 2008; 130: 2667–75. [PubMed: 18237174]

Hansen DF, Yang D, Feng H, Zhou Z, Wiesner S, Bai Y, Kay LE. An exchange-free measure of 15N transverse relaxation: an NMR spectroscopy application to the study of a folding intermediate with pervasive chemical exchange. J Am Chem Soc. 2007; 129: 11468–79. [PubMed: 17722922]

Igumenova TI, Brath U, Akke M, Palmer AG 3rd. Characterization of chemical exchange using residual dipolar coupling. J Am Chem Soc. 2007; 129: 13396–7. [PubMed: 17929930]

Ishima R, Torchia DA. Extending the range of amide proton relaxation dispersion experiments in proteins using a constant-time relaxation-compensated CPMG approach. J Biomol NMR. 2003; 25: 243–8. [PubMed: 12652136]

Jameson G, Hansen AL, Li D, Bruschweiler-Li L, Bruschweiler R. Extreme Nonuniform Sampling for Protein NMR Dynamics Studies in Minimal Time. J Am Chem Soc. 2019; 141: 16829–16838. [PubMed: 31560199]

Karplus M. Aspects of protein reaction dynamics: Deviations from simple behavior. J Phys Chem B. 2000; 104: 11–27.

Karunanithy G, Reinstein J, Hansen DF. Multiquantum Chemical Exchange Saturation Transfer NMR to Quantify Symmetrical Exchange: Application to Rotational Dynamics of the Guanidinium Group in Arginine Side Chains. J Phys Chem Lett. 2020; 11: 5649–5654. [PubMed: 32543198]

Karunanithy G, Yuwen T, Kay LE, Hansen DF. Towards autonomous analysis of chemical exchange saturation transfer experiments using deep neural networks. J Biomol NMR. 2022; 76: 75–86. [PubMed: 35622310]

Korzhnev DM, Neudecker P, Mittermaier A, Orekhov VY, Kay LE. Multiple-site exchange in proteins studied with a suite of six NMR relaxation dispersion experiments: an application to the folding of a Fyn SH3 domain mutant. J Am Chem Soc. 2005; 127: 15602–11. [PubMed: 16262426]

Korzhnev DM, Orekhov VY, Kay LE. Off-resonance R(1rho) NMR studies of exchange dynamics in proteins with low spin-lock fields: an application to a Fyn SH3 domain. J Am Chem Soc. 2005; 127: 713–21. [PubMed: 15643897]

Korzhnev DM, Salvatella X, Vendruscolo M, Di Nardo AA, Davidson AR, Dobson CM, Kay LE. Low-populated folding intermediates of Fyn SH3 characterized by relaxation dispersion NMR. Nature. 2004; 430: 586–90. [PubMed: 15282609]

Lee W, Tonelli M, Markley JL. NMRFAM-SPARKY: enhanced software for biomolecular NMR spectroscopy. Bioinformatics. 2015; 31: 1325–7. [PubMed: 25505092]

Leninger M, Marsiglia WM, Jerschow A, Traaseth NJ. Multiple frequency saturation pulses reduce CEST acquisition time for quantifying conformational exchange in biomolecules. J Biomol NMR. 2018; 71: 19–30. [PubMed: 29796789]

Levitt MH. Symmetrical Composite Pulse Sequences for Nmr Population-Inversion. 2. Compensation of Resonance Offset. J Magn Reson. 1982; 50: 95–110.

Lim J, Xiao TS, Fan JS, Yang DW. An Off-Pathway Folding Intermediate of an Acyl Carrier Protein Domain Coexists with the Folded and Unfolded States under Native Conditions. Angew Chem Int Ed Engl. 2014; 53: 2358–2361. [PubMed: 24470381]

Loria JP, Rance M, Palmer AG. A relaxation-compensated Carr-Purcell-Meiboom-Gill sequence for characterizing chemical exchange by NMR spectroscopy. J Am Chem Soc. 1999a; 121: 2331–2332.

Loria JP, Rance M, Palmer AG. A TROSY CPMG sequence for characterizing chemical exchange in large proteins. J Biomol NMR. 1999b; 15: 151–155. [PubMed: 10605088]

Lundstrom P, Lin H, Kay LE. Measuring 13Cbeta chemical shifts of invisible excited states in proteins by relaxation dispersion NMR spectroscopy. J Biomol NMR. 2009; 44: 139–55. [PubMed: 19448976]

Lundstrom P, Teilum K, Carstensen T, Bezsonova I, Wiesner S, Hansen DF, Religa TL, Akke M, Kay LE. Fractional 13C enrichment of isolated carbons using [1-13C]- or [2- 13C]-glucose facilitates the accurate measurement of dynamics at backbone Calpha and side-chain methyl positions in proteins. J Biomol NMR. 2007; 38: 199–212. [PubMed: 17554498]

Lundstrom P, Vallurupalli P, Hansen DF, Kay LE. Isotope labeling methods for studies of excited protein states by relaxation dispersion NMR spectroscopy. Nat Protoc. 2009; 4: 1641–8. [PubMed: 19876024]

Luz Z, Meiboom S. Nuclear Magnetic Resonance Study of Protolysis of Trimethylammonium Ion in Aqueous Solution - Order of Reaction with Respect to Solvent. Journal of Chemical Physics. 1963; 39: 366.

Massi F, Johnson E, Wang C, Rance M, Palmer AG 3rd. NMR R1 rho rotating-frame relaxation with weak radio frequency fields. J Am Chem Soc. 2004; 126: 2247–56. [PubMed: 14971961]

McConnell HM. Reaction Rates by Nuclear Magnetic Resonance. J Chem Phys. 1958; 28: 430–431.

Milojevic J, Esposito V, Das R, Melacini G. Understanding the molecular basis for the inhibition of the Alzheimer's Aβ-peptide oligomerization by human serum albumin using saturation transfer difference and off-resonance relaxation NMR spectroscopy. J Am Chem Soc. 2007; 129: 4282–4290. [PubMed: 17367135]

Mulder FA, Skrynnikov NR, Hon B, Dahlquist FW, Kay LE. Measurement of slow (micros-ms) time scale dynamics in protein side chains by (15)N relaxation dispersion NMR spectroscopy: application to Asn and Gln residues in a cavity mutant of T4 lysozyme. J Am Chem Soc. 2001; 123: 967–75. [PubMed: 11456632]

Mulder FA, van Tilborg PJ, Kaptein R, Boelens R. Microsecond time scale dynamics in the RXR DNA-binding domain from a combination of spin-echo and off-resonance rotating frame relaxation measurements. J Biomol NMR. 1999; 13: 275–88. [PubMed: 10212986]

Neudecker P, Korzhnev DM, Kay LE. Assessment of the effects of increased relaxation dispersion data on the extraction of 3-site exchange parameters characterizing the unfolding of an SH3 domain. J Biomol NMR. 2006; 34: 129–35. [PubMed: 16604422]

Nielsen JT, Mulder FAA. POTENCI: prediction of temperature, neighbor and pH-corrected chemical shifts for intrinsically disordered proteins. J Biomol NMR. 2018; 70: 141–165. [PubMed: 29399725]

O'Connell NE, Grey MJ, Tang Y, Kosuri P, Miloushev VZ, Raleigh DP, Palmer AG 3rd. Partially folded equilibrium intermediate of the villin headpiece HP67 defined by 13C relaxation dispersion. J Biomol NMR. 2009; 45: 85–98. [PubMed: 19644656]

Palmer AG. NMR characterization of the dynamics of biomacromolecules. Chem Rev. 2004; 104: 3623–3640. [PubMed: 15303831]

Palmer AG. Chemical exchange in biomacromolecules: Past, present, and future. J Magn Reson. 2014; 241: 3–17. [PubMed: 24656076]

Palmer AG 3rd, Koss H. Chemical Exchange. Methods Enzymol. 2019; 615: 177–236. [PubMed: 30638530]

Palmer AG 3rd, Kroenke CD, Loria JP. Nuclear magnetic resonance methods for quantifying microsecond-to-millisecond motions in biological macromolecules. Methods Enzymol. 2001; 339: 204–38. [PubMed: 11462813]

Palmer AG, Massi F. Characterization of the dynamics of biomacromolecules using rotating-frame spin relaxation NMR spectroscopy. Chem Rev. 2006; 106: 1700–1719. [PubMed: 16683750]

Pervushin K, Riek R, Wider G, Wuthrich K. Attenuated T2 relaxation by mutual cancellation of dipole-dipole coupling and chemical shift anisotropy indicates an avenue to NMR structures of very large biological macromolecules in solution. Proc Natl Acad Sci U S A. 1997; 94: 12366–71. [PubMed: 9356455]

Phan IQ, Boyd J, Campbell ID. Dynamic studies of a fibronectin type I module pair at three frequencies: Anisotropic modelling and direct determination of conformational exchange. J Biomol NMR. 1996; 8: 369–78. [PubMed: 20859776]

Press, WH, Flannery, BP, Teukolsky, SA, Vetterling, WT. The Art of Scientific Computing. Second Edition. Cambridge University Press; Cambridge (UK): 1992.

Pritchard RB, Hansen DF. Characterising side chains in large proteins by protonless (13)C-detected NMR spectroscopy. Nat Commun. 2019; 10: 1747. [PubMed: 30988305]

Ramanujam V, Charlier C, Bax A. Observation and Kinetic Characterization of Transient Schiff Base Intermediates by CEST NMR Spectroscopy. Angew Chem Int Ed Engl. 2019; 58: 15309–15312. [PubMed: 31449352]

Rangadurai A, Shi H, Al-Hashimi HM. Extending the Sensitivity of CEST NMR Spectroscopy to Micro-to-Millisecond Dynamics in Nucleic Acids Using High-Power Radio-Frequency Fields. Angew Chem Int Ed Engl. 2020; 59: 11262–11266. [PubMed: 32168407]

Rangadurai A, Szymaski ES, Kimsey IJ, Shi H, Al-Hashimi H. Characterizing micro-to-millisecond chemical exchange in nucleic acids using off-resonance R1ρ relaxation dispersion. Progress in Nuclear Magnetic Resonance Spectroscopy. 2019; 112-113: 55–102. [PubMed: 31481159]

Reddy JG, Pratihar S, Ban D, Frischkorn S, Becker S, Griesinger C, Lee D. Simultaneous determination of fast and slow dynamics in molecules using extreme CPMG relaxation dispersion experiments. J Biomol NMR. 2018; 70: 1–9. [PubMed: 29188417]

Sekhar A, Kay LE. NMR paves the way for atomic level descriptions of sparsely populated, transiently formed biomolecular conformers. Proc Natl Acad Sci U S A. 2013; 110: 12867–74. [PubMed: 23868852]

Sekhar A, Kay LE. An NMR View of Protein Dynamics in Health and Disease. Annu Rev Biophys. 2019; 48: 297–319. [PubMed: 30901260]

Sekhar A, Rumfeldt JAO, Broom HR, Doyle CM, Bouvignies G, Meiering EM, Kay LE. Thermal fluctuations of immature SOD1 lead to separate folding and misfolding pathways. Elife. 2015; 4 e07296 [PubMed: 26099300]

Sekhar A, Vallurupalli P, Kay LE. Folding of the four-helix bundle FF domain from a compact on-pathway intermediate state is governed predominantly by water motion. Proc Natl Acad Sci U S A. 2012; 109: 19268–73. [PubMed: 23129654]

Sekhar A, Velyvis A, Zoltsman G, Rosenzweig R, Bouvignies G, Kay LE. Conserved conformational selection mechanism of Hsp70 chaperone-substrate interactions. Elife. 2018; 7 e32764 [PubMed: 29460778]

Skrynnikov NR, Dahlquist FW, Kay LE. Reconstructing NMR spectra of "invisible" excited protein states using HSQC and HMQC experiments. J Am Chem Soc. 2002; 124: 12352–60. [PubMed: 12371879]

Spector S, Raleigh DP. Submillisecond folding of the peripheral subunit-binding domain. J Mol Biol. 1999; 293: 763–8. [PubMed: 10543965]

Swift T, Connick R. NMR-Relaxation Mechanisms of O17 in Aqueous Solutions of Paramagnetic Cations and the Lifetime of Water Molecules in the First Coordination Sphere. J Chem Phys. 1962; 37: 307–320.

Tiwari VP, Pandit S, Vallurupalli P. Exchangeable deuterons introduce artifacts in amide (15)N CEST experiments used to study protein conformational exchange. J Biomol NMR. 2019; 73: 43–48. [PubMed: 30661150]

Tiwari VP, Toyama Y, De D, Kay LE, Vallurupalli P. The A39G FF domain folds on a volcano-shaped free energy surface via separate pathways. Proc Natl Acad Sci U S A. 2021; 118

Tiwari VP, Vallurupalli P. A CEST NMR experiment to obtain glycine (1)H(alpha) chemical shifts in 'invisible' minor states of proteins. J Biomol NMR. 2020; 74: 443–455. [PubMed: 32696193]

Torchia DA. Dynamics of biomolecules from picoseconds to seconds at atomic resolution. J Magn Reson. 2011; 212: 1–10. [PubMed: 21840740]

Toyama Y, Shimada I. Frequency selective coherence transfer NMR spectroscopy to study the structural dynamics of high molecular weight proteins. J Magn Reson. 2019; 304: 62–77. [PubMed: 31129430]

Trott O, Palmer AG 3rd. R1rho relaxation outside of the fast-exchange limit. J Magn Reson. 2002; 154: 157–60. [PubMed: 11820837]

Tugarinov V, Clore GM. Exchange saturation transfer and associated NMR techniques for studies of protein interactions involving high-molecular-weight systems. J Biomol NMR. 2019; 73: 461–469. [PubMed: 31407202]

Vallurupalli P, Bouvignies G, Kay LE. Increasing the Exchange Time-Scale That Can Be Probed by CPMG Relaxation Dispersion NMR. J Phys Chem B. 2011; 115: 14891–900. [PubMed: 22077866]

Vallurupalli P, Bouvignies G, Kay LE. Studying "invisible" excited protein States in slow exchange with a major state conformation. J Am Chem Soc. 2012; 134: 8148–61. [PubMed: 22554188]

Vallurupalli P, Bouvignies G, Kay LE. A Computational Study of the Effects of C-13-C-13 Scalar Couplings on C-13 CEST NMR Spectra: Towards Studies on a Uniformly C-13-Labeled Protein. Chembiochem. 2013; 14: 1709–1713. [PubMed: 23784752]

Vallurupalli P, Chakrabarti N, Pomes R, Kay LE. Atomistic picture of conformational exchange in a T4 lysozyme cavity mutant: an experiment-guided molecular dynamics study. Chem Sci. 2016; 7: 3602–3613. [PubMed: 30008994]

Vallurupalli P, Hansen DF, Stollar E, Meirovitch E, Kay LE. Measurement of bond vector orientations in invisible excited states of proteins. Proc Natl Acad Sci U S A. 2007; 104: 18473–7. [PubMed: 18006656]

Vallurupalli P, Sekhar A, Yuwen T, Kay LE. Probing conformational dynamics in biomolecules via chemical exchange saturation transfer: a primer. J Biomol NMR. 2017; 67: 243–271. [PubMed: 28317074]

Vallurupalli P, Tiwari VP, Ghosh S. A Double-Resonance CEST Experiment To Study Multistate Protein Conformational Exchange: An Application to Protein Folding. J Phys Chem Lett. 2019; 10: 3051–3056. [PubMed: 31081645]

van Zijl PCM, Yadav NN. Chemical Exchange Saturation Transfer (CEST): What is in a Name and What Isn't? Magn Reson Med. 2011; 65: 927–948. [PubMed: 21337419]

Vugmeyster L, Kroenke CD, Picart F, Palmer AG, Raleigh DP. N-15 R-1 rho measurements allow the determination of ultrafast protein folding rates. J Am Chem Soc. 2000; 122: 5387–5388.

Wang C, Palmer AG. Solution NMR methods for quantitative identification of chemical exchange in 15N-labeled proteins. Magn Reson Chem. 2003; 41: 866–876.

Ward KM, Aletras AH, Balaban RS. A new class of contrast agents for MRI based on proton chemical exchange dependent saturation transfer (CEST). J Magn Reson. 2000; 143: 79–87. [PubMed: 10698648]

Xia Y, Yuwen T, Liu A, Kalodimos CG. Removal of (2)H-decoupling sidebands in (13)CHD(2) (13)C-CEST profiles. J Biomol NMR. 2021; 75: 133–142. [PubMed: 33745068]

Yuwen T, Bouvignies G, Kay LE. Exploring methods to expedite the recording of CEST datasets using selective pulse excitation. J Magn Reson. 2018; 292: 1–7. [PubMed: 29753980]

Yuwen T, Kay LE. A new class of CEST experiment based on selecting different magnetization components at the start and end of the CEST relaxation element: an application to (1)H CEST. J Biomol NMR. 2018; 70: 93–102. [PubMed: 29352366]

Yuwen T, Kay LE. Revisiting (1)H(N) CPMG relaxation dispersion experiments: a simple modification can eliminate large artifacts. J Biomol NMR. 2019; 73: 641–650. [PubMed: 31646421]

Yuwen T, Kay LE, Bouvignies G. Dramatic Decrease in CEST Measurement Times Using Multi-Site Excitation. Chemphyschem. 2018; 19: 1707–1710. [PubMed: 29663694]

Yuwen T, Sekhar A, Kay LE. Separating dipolar and chemical exchange magnetization transfer processes in [1]H-CEST. Angew Chem Int Ed Engl. 2017; 56: 6122–6125. [PubMed: 28035783]

Yuwen T, Vallurupalli P, Kay LE. Enhancing the Sensitivity of CPMG Relaxation Dispersion to Conformational Exchange Processes by Multiple-Quantum Spectroscopy. Angew Chem Int Ed Engl. 2016; 55: 11490–4. [PubMed: 27527986]

Zhao B, Baisden JT, Zhang Q. Probing excited conformational states of nucleic acids by nitrogen CEST NMR spectroscopy. J Magn Reson. 2020; 310 106642 [PubMed: 31785475]

Zhao B, Guffy SL, Williams B, Zhang Q. An excited state underlies gene regulation of a transcriptional riboswitch. Nat Chem Biol. 2017; 13: 968–974. [PubMed: 28719589]

Zhou Y, Yang DW. Effects of J couplings and unobservable minor states on kinetics parameters extracted from CEST data. J Magn Reson. 2014; 249: 118–125. [PubMed: 25462955]

Zhuravleva A, Korzhnev DM. Protein folding by NMR. Prog Nucl Magn Reson Spectrosc. 2017; 100: 52–77. [PubMed: 28552172]

Zwanzig R. Simple model of protein folding kinetics. Proc Natl Acad Sci U S A. 1995; 92: 9801–4. [PubMed: 7568221]

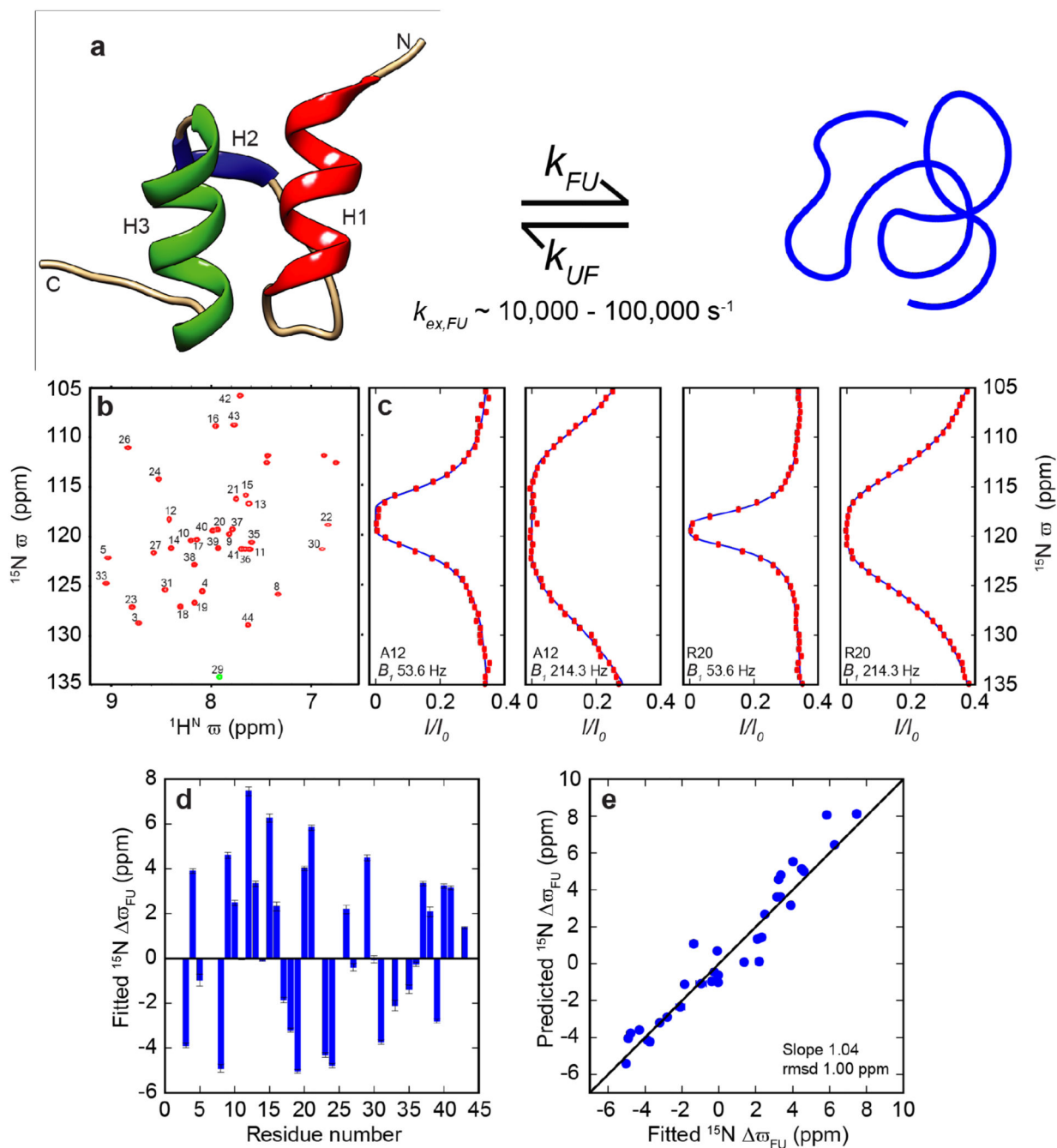Zwanzig R, Szabo A, Bagchi B. Levinthal's paradox. Proc Natl Acad Sci U S A. 1992; 89: 20–2. [PubMed: 1729690]

Fig. 1. Amide ^{15}N CEST detects sparsely populated states with ~100 μs lifetimes.
a) At 42.9 °C the folded structure of PSBD [PDB: 1W3D (Allen et al., 2005)] that consists of three helices exchanges with the unfolded (U) state populated to < 5% on the ~100 μs timescale. **b)** The 700 MHz amide ^{15}N-$^{1}H^{N}$ correlation map of U-[^{15}N] PSBD (42.9 °C) is well resolved and contains only correlations arising from the folded (F) state. Peaks are labeled according to the residue from which they arise. It should be noted that peak-positions do not strictly correspond to the F state but are shifted towards the U state as the system is in fast exchange between the F and U states. **c)** ^{15}N CEST intensity profiles from

A12 and R20. Experimental data is represented using filled red circles and the blue line is calculated using best-fit parameters (p_U = 3.9% and $k_{ex,FU}$ = 11363 s^{-1}). **d)** Large variations are observed in the ^{15}N CEST derived ϖ_{FU} values along the length of the sequence. **e)** The ^{15}N CEST derived ϖ_{FU} values are in excellent agreement with the predicted ϖ_{FU} values. ϖ_U values to calculate ϖ_{FU} were obtained using the program POTENCI (Nielsen and Mulder, 2018).
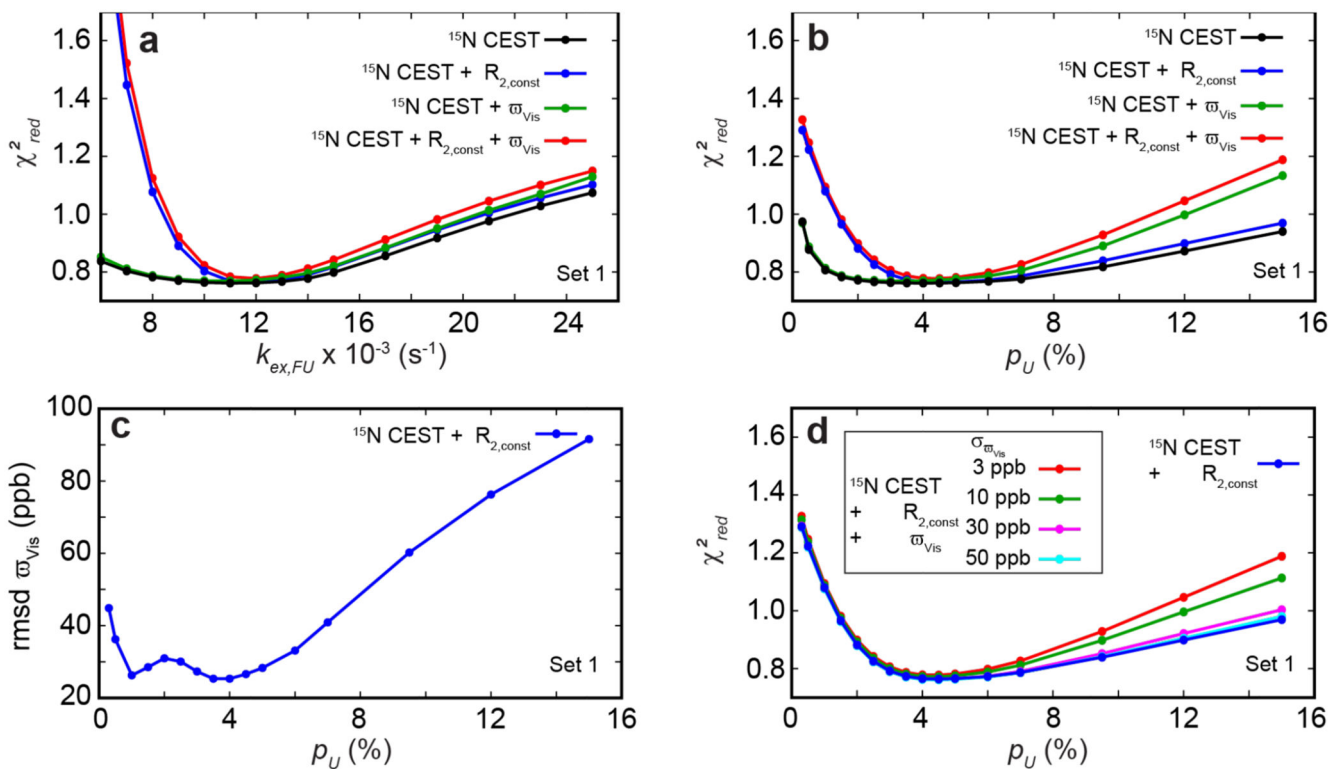
Fig. 2.
Experimentally derived constraints ($R_{2,const}$) on $R_{2,F}$ values and the inclusion of accurate ϖ_{Vis} shifts in the analysis of amide ^{15}N CEST data leads to pronounced minima in the **(a)** χ^2_{red} versus $k_{ex,FU}$ and **(b)** χ^2_{red} versus p_U plots. In **(a)** and **(b)** best-fit calculations performed using only ^{15}N CEST data is shown in black, calculations performed using $R_{2,F}$ constraints ($R_{2,const}$) are shown in blue, calculations performed with the addition of only ϖ_{Vis} shifts are shown in green and calculations performed using both $R_{2,F}$ constraints and ϖ_{Vis} shifts are shown in red. **(c)** Root mean square deviation (rmsd) between the measured ϖ_{Vis} shifts and those calculated from parameters obtained from best-fit calculations using ^{15}N CEST data and $R_{2,F}$ constraints (blue in (b)) plotted as a function of p_U. **(d)** Variation of the χ^2_{red} versus p_U plots as a function of precision in the ϖ_{Vis} shifts. Best-fit calculations were performed using ^{15}N CEST with $R_{2,F}$ constraints while artificially increasing the uncertainty ($\sigma\varpi_{Vis}$) on the measured ϖ_{Vis} shifts from 3 to 50 ppb. For reference the results of the optimization performed without ϖ_{Vis} shifts but including $R_{2,F}$ constraints (blue in b) is shown in blue. The calculations were performed by globally analyzing data from 18 residues (Set 1) for which | ϖ_{FU}| 3 ppm.
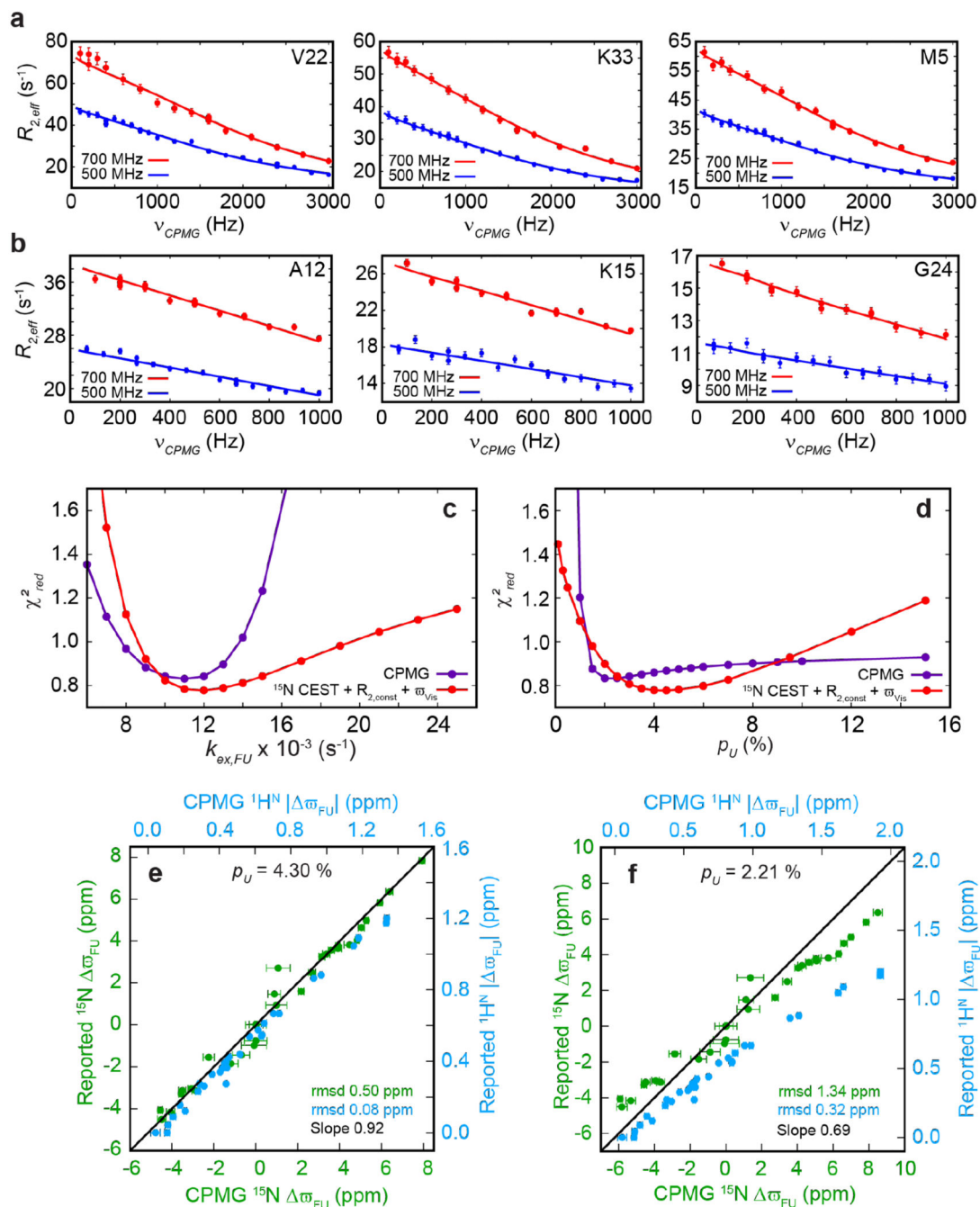
Fig. 3.

CPMG data is consistent with exchange parameters obtained from the analysis of ^{15}N CEST data. Representative $^1H^N$ (**a**) and ^{15}N (**b**) CPMG relaxation dispersion profiles recorded at 500 and 700 MHz. The experimental data is represented using filled circles while the line is calculated using the best-fit parameters ($p_U = 2.21\%$ and $k_{ex,FU} = 10987$ s^{-1}). (**c**) χ^2_{red} versus $k_{ex,FU}$ and (**d**) χ^2_{red} versus p_U plots obtained using $^1H^N$ & ^{15}N CPMG data (purple) and ^{15}N CEST data (red) along with ϖ_{Vis} shifts and constraints on $R_{2,F}$ values. The minima in the χ^2_{red} versus $k_{ex,FU}$ curves (**c**) are consistent with one another, while the χ^2_{red} versus p_U

curve derived from the CPMG data does not have a convincing minimum except for a small spurious one at 2.21% **(d)**. Comparison between the reported $^1\text{H}^N|\varpi_{FU}|$ and $^{15}\text{N}\ \varpi_{FU}$ values and those obtained here by setting p_U to 4.3% **(e)** and 2.21% **(f)**. In **(e)** and **(f)** the combined slopes were calculated for $^1\text{H}^N|\varpi_{FU}|$ and $^{15}\text{N}\ \varpi_{FU}$ values by multiplying the $^1\text{H}^N|\varpi_{FU}|$ values by 10.
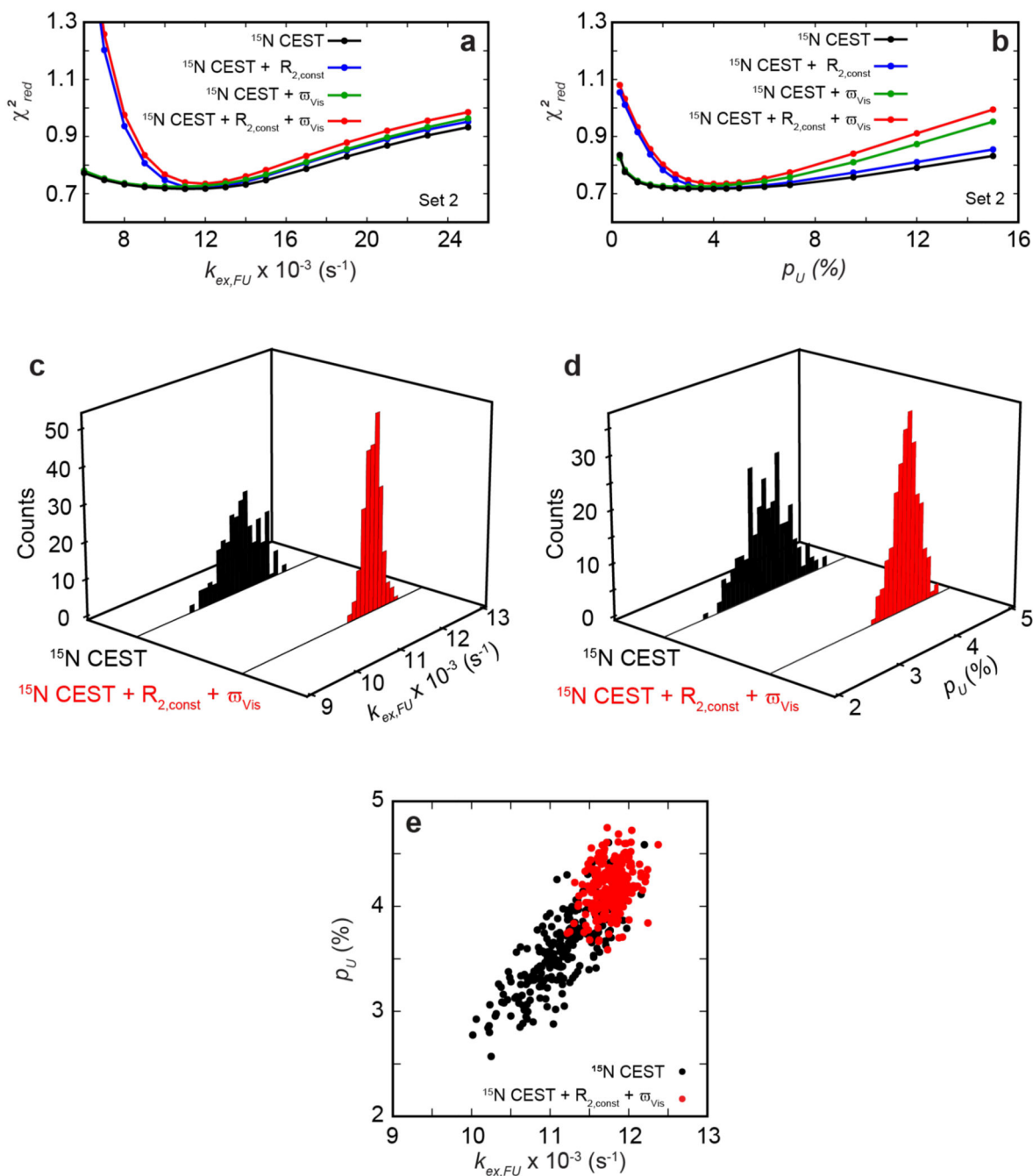
Fig. 4.

Experimentally derived constraints ($R_{2,const}$) on $R_{2,F}$ values and the inclusion of accurate ϖ_{Vis} shifts during data analysis has a large effect on the exchange parameters extracted by analysing ^{15}N CEST data from the Set 2 residues (5 ppm $\mid \varpi_{FU} \mid$ 3 ppm). **(a)** and **(b)** were computed exactly as in Fig 2a and Fig 2b respectively, but using only the 14 Set 2 residues. Distribution of $k_{ex,FU}$ **(c)** and p_U **(d)** values obtained from 250 bootstrap trials using only ^{15}N CEST data (black) and using both $R_{2,F}$ constraints and ϖ_{Vis} shifts in addition

to ^{15}N CEST data (red). **e)** Scatter plot showing different $k_{ex,FU}$ and p_U values obtained in the bootstrap trials.
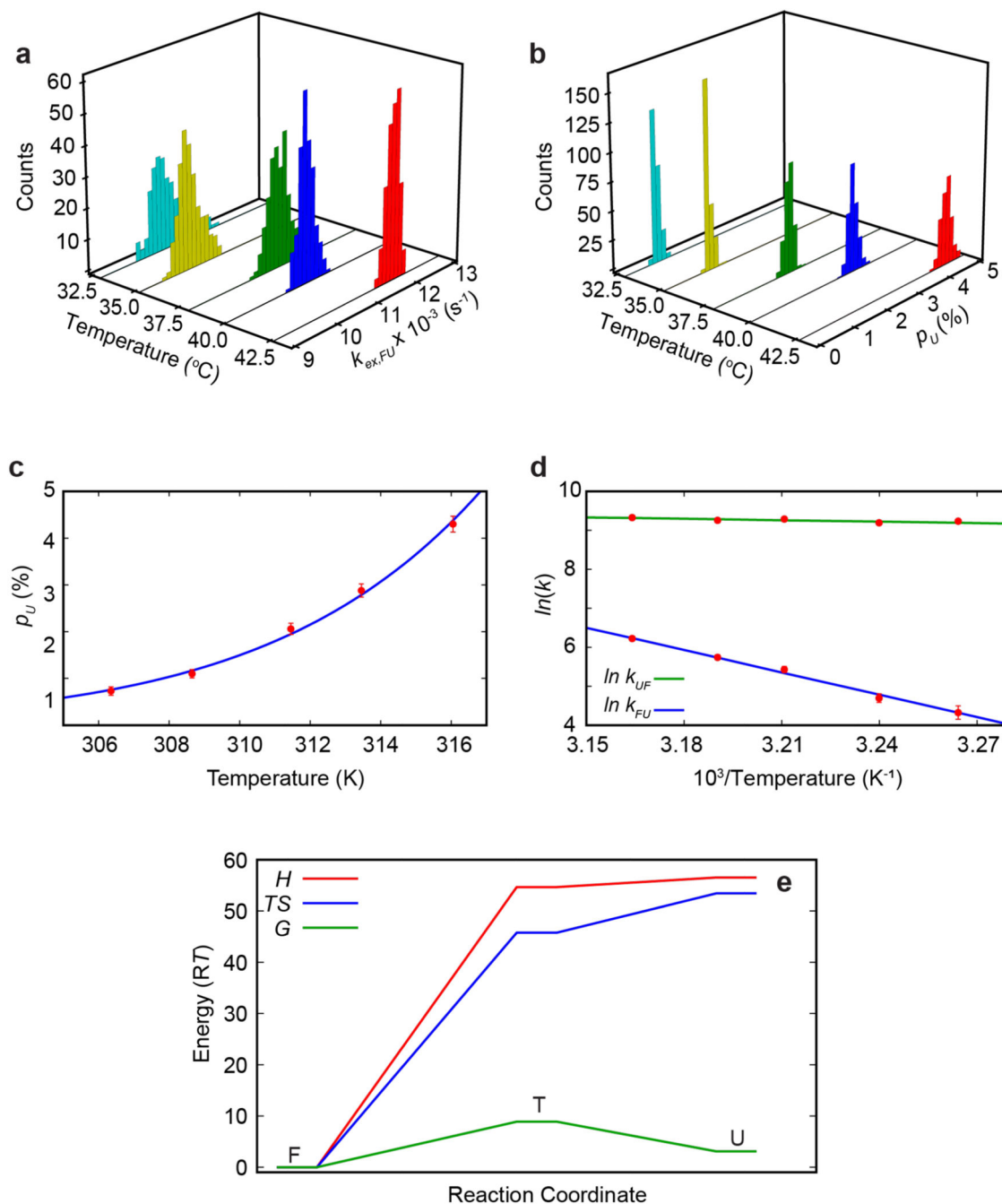
Fig. 5.

Understanding the PSBD folding/unfolding reactions. Distribution of $k_{ex,FU}$ (**a**) and p_U (**b**) values obtained from 250 bootstrap trials at various temperatures (33.2 to 42.9 °C). The exchange parameters (Table 1) were obtained from ^{15}N CEST data supplemented with $R_{2,F}$ constraints and ϖ_{Vis} shifts. van't Hoff (**c**) and Arrhenius (**d**) plots of exchange parameters obtained at different temperatures. As described in Materials and Methods, the thermodynamic (ΔH_{UF} and ΔS_{UF}) and activation (ΔH_{UF}^{*} and ΔS_{UF}^{*}) parameters were obtained using the data shown in the Arrhenius plots (d). The van't Hoff plot (c) is shown

here to illustrate how p_U increases with temperature and the best-fit H_{UF} and S_{UF} values obtained in (d) were used to generate the blue line. **e)** Decomposition of the Gibbs free energy (G) for the U and T states into its enthalpic (H), and entropic (TS) components. H and S are set to 0 for state F. The reference temperature in **(e)** is 316.05 K.

Table 1

Summary of various parameters obtained from the global two-state (F$\rightleftharpoons$U) modeling of ^{15}N CEST recorded on PSBD at various temperatures. Set 1 refers to 18 residues with | ϖ_{FU}| 3 ppm at 42.9 °C. Set 2 refers to 14 residues for which: 3 ppm | ϖ_{FU}| 5 ppm. See materials and methods for a list of the residues contained in sets 1 and 2. Columns titled R$_{2,const}$ and ϖ_{Vis} shifts are respectively used to indicate if experimentally derived constraints on $R_{2,F}$ values (R$_{2,const}$) or ϖ_{Vis} shifts were included in the analysis.

S No	Temperature (°C)	Residue Set	R$_{2,const}$	ϖ_{Vis}	$k_{ex,FU}$ (s^{-1})	p_U (%)	χ^2_{red}
1	42.9	Set 1	No	No	11317 ± 376	4.00 ± 0.32	0.76
2	42.9	Set 1	Yes	No	11688 ± 142	4.43 ± 0.20	0.77
3	42.9	Set 1	No	Yes	10592 ± 387	3.23 ± 0.31	0.77
4	42.9	Set 1	Yes	Yes	11739 ± 147	4.30 ± 0.17	0.78
5	42.9	Set 2	No	No	11189 ± 421	3.61 ± 0.38	0.72
6	42.9	Set 2	Yes	No	11654 ± 179	4.19 ± 0.21	0.72
7	42.9	Set 2	No	Yes	11458 ± 454	2.83 ± 0.37	0.73
8	42.9	Set 2	Yes	Yes	11788 ± 194	4.14 ± 0.22	0.74
9	40.3	Set 1	Yes	Yes	10788 ± 183	2.88 ± 0.14	0.86
10	38.3	Set 1	Yes	Yes	11046 ± 240	2.06 ± 0.12	0.94
11	35.5	Set 1	Yes	Yes	9974 ± 262	1.10 ± 0.09	0.99
12	33.2	Set 1	Yes	Yes	10331 ± 379	0.73 ± 0.09	1.05